Understanding Reactivity and Assembly of Dichalcogenides: Structural, Electrostatic Potential, and Topological Analyses of 3 H-1,2-Benzodithiol-3-one and Selenium Analogs

R. Shukla, A. Dhaka, Emmanuel Aubert, V. Vijayakumar-Syamala, O. Jeannin, M. Fourmigué, Enrique Espinosa

Understanding Reactivity and Assembly of Dichalcogenides: Structural, Electrostatic Potential and Topological Analyses of 3*H*-1, 2-Benzodithiol-3-one and Se Analogs

Rahul Shukla,[†] Arun Dhaka,[‡] Emmanuel Aubert,[†] Vishnu Vijayakumar-Syamala,[†] Olivier Jeannin,[‡] Marc Fourmigué*,[‡] and Enrique Espinosa*,[†]

[†] *Université de Lorraine, CNRS, CRM2, F-54000 Nancy, France. E-mail: enrique.espinosa@univ-lorraine.fr*

[‡] *Université de Rennes, CNRS, ISCR (Institut des Sciences Chimiques de Rennes), UMR 6226, Campus de Beaulieu, F-35042 Rennes, France. E-mail: marc.fourmigue@univ-rennes1.fr*

Abstract

Molecular assembly and reactivity have been investigated with a series of 3H-1,2-benzodithiol-3-(thi)one derivatives and their (mixed) selenated analogs. Electrostatic potential calculations on monomers show three σ-hole regions around the dichalcogenide Ch–Ch bond (Ch = S, Se), one side-on and two along the bonding direction. The topological analysis of the electron density $\rho(\mathbf{r})$ points the weak nature of the Ch–Ch bond. σ-hole and lone-pair regions are described in terms of charge depletion (CD) and charge concentration (CC) sites found in the valence shell of chalcogen atoms. Whereas CD and CC sites are characterized by the topological critical points of $L(\mathbf{r}) = -\nabla^2\rho(\mathbf{r})$, their electrophilic and nucleophilic power are measured by the corresponding L/ρ magnitudes. In crystal structures, each chalcogen bond (ChB) involves a σ-hole region and shows a CD···CC interaction that aligns with the internuclear direction of the atoms the CD and CC sites belong. The alignment holds simultaneously for all of the ChB interactions in each crystal structure, indicating that CD···CC interactions drive molecular orientation in molecular assembly. Strength of ChB is measured in terms of the topological properties of $\rho(\mathbf{r})$, whereas the intensity of the electrophilic…nucleophilic interaction is monitored by $[(L/\rho)_{CC} - (L/\rho)_{CD}]/d^2_{CC...CD}$. The σ-hole in side-on conformation forms the strongest ChB interactions in molecular assembly. Reactivity of molecules against nucleophilic attack has been investigated along each of the three σ-hole regions by using fluoride as a probe. Adducts formed along the Ch–Ch bonding direction are energetically more favorable than in side-on conformation. At optimized geometries, the

F···Ch bond (Ch = S, Se) exhibits a partial covalent character, while it weakens concomitantly the Ch···Ch bond that also becomes of partial covalent character. In the reactivity process, the significant reorientation of the plane containing the chalcogen *lone-pairs*, along with the opening, shrinking and splitting of reactivity surfaces $\nabla^2\rho(\mathbf{r}) = 0$, is the signature of the charge redistribution that involves the nucleophilic attack.

■ INTRODUCTION

Interest for the chemistry of selenium is currently experiencing a strong revival along two different directions,[1] (i) pharmaceutical applications of selenium-containing molecules and more recently, (ii) involvement of organo-selenium derivatives as chalcogen bond donors in noncovalent σ-hole based interactions.[2,3] For example, the ebselen molecule [2-phenyl-1,2-benzoisoselenazol-3(2H)one], which functions as an antioxidant, has inspired a worldwide interest in the design of glutathione peroxidase (GPx) mimics. Besides, analysis of the charge density around Se−N and Se−C covalent bonds in conjunction with the Se•••O chalcogen bonding modes in ebselen and its analogues provided insights into the mechanism of drug action in this class of organoselenium antioxidants.[4] Selenium atoms activated by electron-withdrawing groups as in organic selenocyanates[5] or in diselenides[6] were recently shown to act as efficient chalcogen bond donors through the electropositive area (σ-hole) they develop in the prolongation of the covalent bonds to selenium. They are also involved in the glutathione peroxidase (GPx)-like catalytic activity of ebselen.[7] Organoselenium derivatives are also used as reagents in synthesis and one can mention here electrophilic reagents such as N-phenylselenophthalimide for phenylselenation.[8]

In the course of our investigations of diselenide derivatives as chalcogen bond donors,[6] we were attracted by the 3H-benzo[1,2]dithiole-3-one and 3H-benzo[1,2]dithiole-3-thione heterocycles and their selenium analogs shown in Scheme 1 with the abbreviations used in the following. Most of them have been reported (except 3*H*-1,2-benzodiselenol-3-thione, **CSSeSe**), either as reagent or reagent precursor in organic synthesis or biochemistry, or for their pharmaceutical interest based on their antioxidant activity.[9] They also bear some analogy with selenium based molecules (selenophtalic anhydride,[10] diselenides,[6] tellurophenes[11,12] and selenophenes,[13] organic selenocyanates[5,14,15]) where proper activation of the Se atom leads to the formation of strong electron-depleted area in the prolongation of the two covalent bonds to Se, known as σ-holes (Scheme 1a). We can distinguish potentially here two types of σ-holes, those in the prolongation of the covalent Ch2−Ch3 (Ch2, Ch3 = S, Se) bond, noted R1A and R1B in Scheme 1a, and those in the prolongation of the C−Ch2/Ch3 bonds, merging in the R2 region shown in Scheme 1a. These sites are thought to control not only the initial reactivity of such molecules toward nucleophilic attack, but also their solid-state arrangement as they can interact preferentially with charge-concentrated area of the same molecules (oxygen/chalcogen lone pairs), or with Lewis bases in co-crystals.

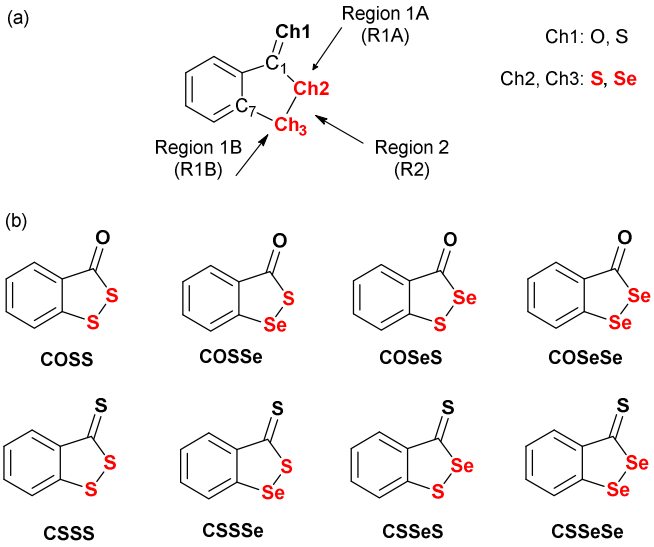

Scheme 1. (a) Possible σ-hole Regions around the Dichalcogenide Ch2–Ch3 Bond in the 1,2-Dichalcogenole series (b) Molecular Structures of Investigated Compounds.

For instance, in the carbonyl series, 3*H*-1,2-benzodithiol-3-one (**COSS)** and 3*H*-1,2-benzoselenathiol-3-one (**COSSe)** have recently been shown to be very good precursors for the synthesis of persulfides (RSSH), selenylsulfides (RSeSH) and hydrogen sulphide (H_2S), with ring opening between the C=O and SS (or SSe) moieties.[16] Similarly, the reaction of **COSS** with sp^2 nitrogen nucleophiles selectively opens the heterocycle on the same site. This reactivity toward nucleophiles of specifically the C1–Ch2 bond raises several questions, if one considers the potentially much weaker Ch2–Ch3 (S–S, S–Se, Se–Se) dichalcogenide bond.

Note also that the oxidation of **COSS** in the presence of H_2O_2,[17] peracetic acid[18] or dimethyloxirane[19,20] selectively affords the 1-oxide (or the 1,1-dioxide known as Beaucage reagent).[21,22] 3*H*-1,2-Benzothiaselenol-3-one (**COSeS**) is also known as an efficient reagent for stereospecific selenization of *H*-phosphates and *H*-phosphonothioate diesters to afford Se-derivatized RNAs, DNAs and proteins,[23,24] an important issue to overcome the problems faced in their X-ray crystallographic studies.[25] It is also reported as a potent fungicide at 1 ppm and shows herbicidal and insecticidal activity at higher concentrations.[26] Finally, **COSeSe** is only mentioned once in the literature for its activity toward on lysosomes and mitochondria *in vitro*, without any details on its synthesis.[27]

Furthermore, none of the four *carbonyl* derivatives, i.e. **COSS**, **COSSe**, **COSeS** and **COSeSe** has been structurally characterized while the electron-withdrawing carbonyl group is expected to favor a polarization of the Ch2–Ch3 bond and peculiar electrostatic potential distribution which could favor chalcogen bonding interactions in the solid state with both Ch2

and Ch3 chalcogens acting as ChB donors. Furthermore, at variance with most reported diselenides investigated as ChB donors which are symmetric (R−Se−Se−R' with R = R'),[6] the compounds investigated here are not, and thus raise the question of the location of the "deepest" σ-holes, between the R1A, R1B and R2 regions.

In the thiocarbonyl series, X-ray crystal structures have been reported for the three **CSSS**, **CSSSe** and **CSSeS** derivatives (**CSSeSe** is unknown). The 1,2-dithiole derivative **CSSS** exhibits a reactivity comparable to **COSS**, with ring opening between the C=S and S−S moieties, by sp^2 nitrogen nucleophiles[28] or by active methylene compounds,[29] or with selective oxidation by H_2O_2 into the 1-oxide.[17]

The work described here aims at rationalizing *both* the specific reactivity and the molecular assembly in the solid-state structures of these series of compounds, as models for many others involving a disulfide or diselenide bond. For that purpose, we have synthetized six of these eight derivatives. We then combine the determination of their crystal structures and analysis of the most pertinent interactions, with specific emphasis on chalcogen bonding since it is actually present in all of them. This will be substantiated by a thorough theoretical investigation of the electronic density distribution $\rho(\mathbf{r})$ and its properties (electrostatic potential and topological analyses of $\rho(\mathbf{r})$ and $L(\mathbf{r}) = -\nabla^2\rho(\mathbf{r})$) around the dichalcogenide bond. First, this will be carried out with optimized monomers, aimed at unraveling the location of σ-hole regions and the most electrophilic chalcogen atoms within the series, as a rationale for their molecular assembly and chemical reactivity. In a second step, intermolecular chalcogen bonding interactions (ChB) will be analyzed in terms of the topological properties of $\rho(\mathbf{r})$ at bond critical points (BCP) between interacting atoms in dimers extracted from the crystal structures, together with the distribution of $L(\mathbf{r}) = -\nabla^2\rho(\mathbf{r})$ magnitudes and the associated critical points (CP's) in the regions where ChB show. Finally, the reactivity of this series of 1,2-dichalcogenoles will be investigated in terms of the energetic stability and $\rho(\mathbf{r})$ properties of their fluoride adducts, with F^- at proximity of the dichalcogenide bond in regions where σ-holes show. The small size of F^- allows indeed for minimum steric hindrance, while the anionic character of F^- results in substantial nucleophilic capacity.

■ RESULTS AND DISCUSSION

Syntheses. As shown in Scheme 2, the preparation of all molecules is based on the chalcogenation/cyclization of 2,2'-dithiosalicylic acid or 2,2'-diselenosalicylic acid. Indeed, treatment of 2,2'-dithiosalicylic acid with P_4S_{10} in dioxane affords **CSSS** in 93% (at variance with the reported procedure performed in xylene with 80% yield).[30] Reaction of **CSSS** with mercuric acetate gives **COSS** in 82% yield, a more direct route than that reported from the successive treatment of **CSSS** with tetrachloro-o-benzoquinone and HCl in dioxane.[31] Note that **COSS** had been also obtained by sulfuration of 2-halobenzoic acid phenyl ester (obtained from 2-halo-benzoic acid) with Na_2S_2.[32,33]

Selenation of 2,2'-dithiosalicylic acid to afford **COSeS** has been performed with $Ph_3P{=}Se$, following a reported procedure.[23] This reagent appears easier to handle than the reported (phenylseleno)phosphonic dichloride in the presence of pyridine.[24] It was therefore used also for the selenation of 2,2'-diselenosalicylic acid to afford the **COSeSe**, albeit in limited yield (10%). Note that the only mention of **COSeSe** does not report its synthesis. The sulfuration of 2,2'-diselenosalicylic acid with P_4S_{10} in dioxane gives **CSSSe** in 80% yield. This route differs from that reported earlier where the already formed **COSeSe** was treated with P_4S_{10} in CS_2.[34] **CSSeS** was already reported and structurally characterized.[35] Only the thiocarbonyl diselenide **CSSeSe** is still unknown.

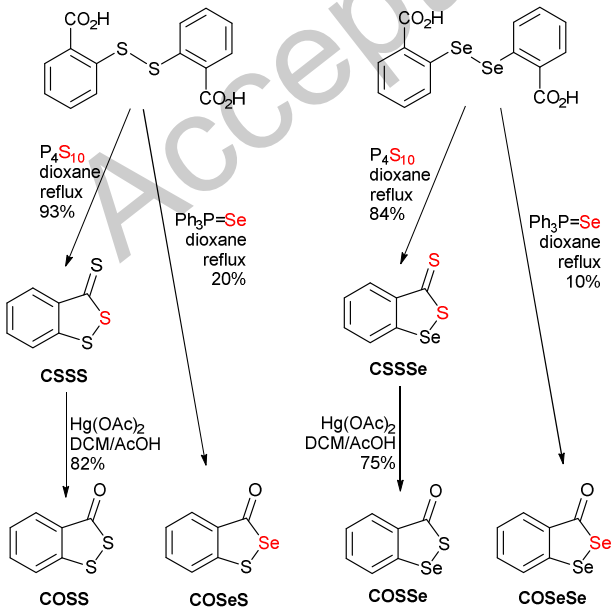

Scheme 2. Synthetic Procedures

Computational Details and Topological Analyses of $\rho(\mathbf{r})$ and $L(\mathbf{r}) = -\nabla^2\rho(\mathbf{r})$.

Geometry optimizations, frequency calculations and topological investigations on (i) optimized monomers, (ii) dimers extracted from the crystal structures, and (iii) anionic fluoride adducts were performed at the B3LYP-D3/aug-cc-pVTZ level of theory. The electrostatic potential (ESP) maps were plotted for the monomers on the 0.001 and 0.002 a.u. electron density isosurfaces. The topological analyses of the electron density $\rho(\mathbf{r})$ and its negative Laplacian $L(\mathbf{r}) = -\nabla^2\rho(\mathbf{r})$ were performed with the AIMALL software.[36] Gaussian09 (version D.01) software package was used for optimization and frequency calculations.[37]

Within the framework of the Quantum Theory of Atoms in Molecules (QTAIM) developed by Bader and co-workers,[38] the topological analysis of $\rho(\mathbf{r})$ permits to identify any bonding interatomic interaction by the formation of a bond path between atoms. Along this path $\rho(\mathbf{r})$ is maximum with respect to any other direction linking the nuclei. Bond critical points $\mathbf{r}_b$ (BCPs) are placed at the intersection of bond paths and interatomic surfaces (namely, the zero-flux surfaces of $\rho(\mathbf{r})$ enclosing the atomic basins). The intensity and nature of pairwise interactions are determined by analyzing simultaneously the topological properties of $\rho(\mathbf{r})$ at $\mathbf{r}_b$'s. Hence, while ρ_b and $\nabla^2\rho_b$ measure the quantity of charge density and the local depletion ($\nabla^2\rho_b > 0$) or concentration ($\nabla^2\rho_b < 0$) of $\rho(\mathbf{r})$ at $\mathbf{r}_b$, the local electron potential (V_b) and kinetic (G_b) energy densities are interpreted as the pressures exerted to localize and to deplete the electron distribution at the interatomic surface.[39] The ratio $|V_b|/G_b$ is a very useful descriptor to distinguish between *pure* closed-shell interactions ($|V_b|/G_b<1$), shared-shell interactions ($|V_b|/G_b >2$), and intermediate interactions with a partial (starting) covalence degree ($1< |V_b|/G_b<2$) where a local depletion of $\rho(\mathbf{r})$ ($\nabla^2\rho_b > 0$) is still observed.[40] Thus, the stronger the interaction the larger ρ_b , V_b and $|V_b|/G_b$ quantities become, while $|V_b|/G_b$, and $\nabla^2\rho_b$ monitor the nature of the interaction and the subtle effects in its evolving behavior.

The $L(\mathbf{r}) = -\nabla^2\rho(\mathbf{r})$ function points out the regions of the space where the electronic charge is locally concentrated ($L(\mathbf{r}) > 0$) and depleted ($L(\mathbf{r}) < 0$). The $L(\mathbf{r})$ function has been proposed as the physical basis for the *VSEPR* model,[41,42] and the iso-surface $L(\mathbf{r}) = 0$ has been defined as the reactivity surface of molecules undergoing a nucleophilic attack (the holes observed in the surface mark the regions through which the attack can take place).[38] The topological analysis of $L(\mathbf{r})$ carries the characteristic critical points (CPs) of the function. While (3,−3) and (3,+3) CPs indicate local maxima (3D-concentration) and minima (3D-depletion) of electronic charge, (3,−1) and (3,+1) CPs are saddle points and correspond respectively to local 1D-depletion/2D-concentration and 2D-depletion/1D-concentration along the three main

directions of the L-distribution at CP. Because the $L(\mathbf{r})$ distribution exhibits positive and negative values, and varies rapidly in the space, the topology of $L(\mathbf{r})$ is difficult to interpret. In particular, many CPs of all types exhibit around atoms and care should be taken in the selection of the relevant ones for discussions involving nucleophilic (charge concentration, CC) and electrophilic (charge depletion, CD) sites. As shown in previous studies,[10,43] the electrophilic/nucleophilic power of CD/CC sites can be monitored by the L/ρ value at the corresponding sites (normalizing by ρ permits the comparison between atoms with a different number of electrons). Thus, the larger the positive/negative L/ρ magnitude the more nucleophilic/electrophilic power of the site.

The methodology based on the topology and the distribution of $L(\mathbf{r})$ has proved to be very useful in describing different electrophilic-nucleophilic interactions.[10,43-49] Hence, using the L/ρ parameter, the quantity $\Delta(L/\rho) = (L/\rho)_{CC} - (L/\rho)_{CD}$ aims to evaluate the CC…CD interaction. Accordingly, the larger the positive difference $\Delta(L/\rho) = (L/\rho)_{CC} - (L/\rho)_{CD}$ the more important is the nucleophilic•••electrophilic interaction.[10,43] To monitor the intensity of the electrophilic•••nucleophilic interaction we introduce in this work the descriptor $\Delta(L/\rho)/d^2_{CD\cdots CC} = [(L/\rho)_{CC} - (L/\rho)_{CD}]/d^2_{CD\cdots CC}$, where $d_{CD\cdots CC}$ is the CD•••CC distance. The descriptor increases with the electrophilic and the nucleophilic power of the sites, and with shorter distances. Therefore, the larger is the positive value of $\Delta(L/\rho)/d^2_{CD\cdots CC}$ the most relevant is the interaction. A more detailed description on the $L(\mathbf{r})$ function and its topology is provided in section S1 of the supporting information.

Geometrical Description of the Chalcogen Bond.

The relative orientation of two atoms involved in a chalcogen bond (or any other noncovalent interaction) is very crucial to understand the electrophilic-nucleophilic behavior of the interaction. In the crystal structures discussed here, we observe two cases of chalcogen bonding interactions, namely $Ch_{sp^3}(\delta^+)\cdots Ch_{sp^2}(\delta^-)$ and $Ch_{sp^3}(\delta^+)\cdots Ch_{sp^3}(\delta^-)$. In Figure 1, ζ_1 corresponds to angles with regard to the Ch-atom acting as electrophile (left side moiety: $X\text{-}Ch_{left}\cdots Ch_{rigth}$), whereas ζ_2 corresponds to angles with regard to the Ch-atom acting as nucleophile (right side moiety: $Ch_{left}\cdots Ch_{right}\text{-}Y$). Interactions between sp^3 and sp^2 hybridized chalcogen atoms are angularly described by two ζ_1 angles (ζ_{1A} and ζ_{1B}) and one ζ_2 angle (Figure 1, left), whereas for interactions involving two sp^3 hybridized chalcogen atoms it results in two ζ_1 angles (ζ_{1A} and ζ_{1B}) and two ζ_2 angles (ζ_{2A} and ζ_{2B}) (Figure 1, right).

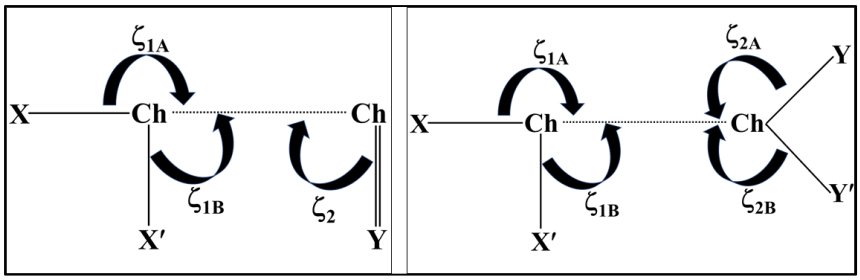

Figure 1. Representation of ζ_1 and ζ_2 angles considered for (left) Ch_{sp^3}•••Ch_{sp^2} and (right) Ch_{sp^3}•••Ch_{sp^3} chalcogen bonding interactions. Ch = Chalcogen atom, X/X′/Y/Y′ = Any atom.

Intermolecular Interactions and Crystal Packing. *Overall Description of Crystal Structures.* Crystal structures of the prepared compounds were determined from single crystal X-ray diffraction. **COSS** crystallizes in the monoclinic system, space group $P2_1/c$, with two molecules in the asymmetric unit [marked A and B in Fig. 2(a)]. Both **COSeS** and **COSeSe** were found to be isostructural with **COSS** [Figure S1-S3]. Note that positional disorder observed between carbonyl and S-Se bond in **COSeS** was solved with the two positions in a 95:5 relative occupancy. For the discussion on crystal packing and intermolecular interactions in **COSeS** we only utilized the major component of the disorder. Analysis of crystal packing of these three crystal structures reveals the formation of ····AABBAABB···· chains, running along the ***a*+*b*** and ***a*-*b*** directions [Figure 2(a), Figure S1-S3]. These chains are stabilized primarily by three unique π···π stacking motifs (namely AA, AB, BB) with the molecular centroid-centroid distances in the range of 3.6 – 3.9 Å [Figure 2(a), Table S1]. The centroid-centroid distance tends to increase from **COSS** to **COSeSe** molecules. While ····AABBAABB···· chains are parallel along each ***a*+*b*** and ***a*-*b*** direction, they are perpendicularly oriented in alternated way along the ***c***-axis [Figure 2(a), Figures S1-S3]. These π-stacking molecular chains are assembled to each other by hydrogen bonding (C-H···O, C-H···π, C-H···S and/or C-H···Se) and chalcogen bonding (Ch···Ch'; Ch = S, Se; Ch' = O, S) interactions (Table S2), thus generating the 3D network of the crystal structure [Figure S1-S3].

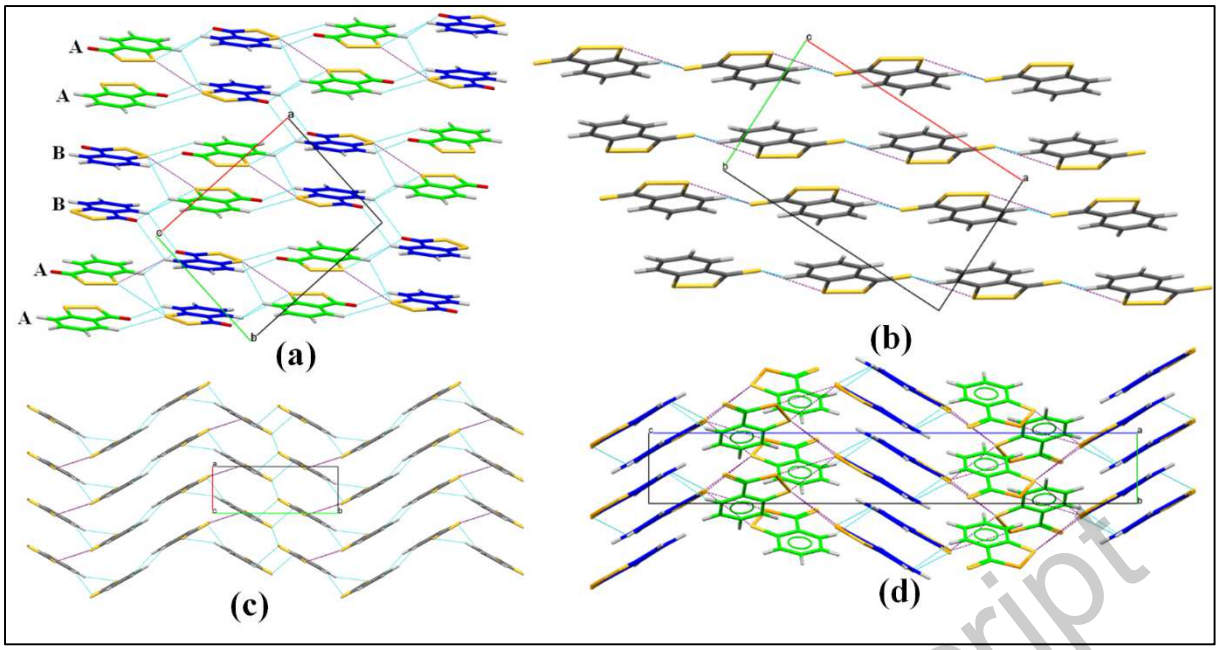

Figure 2. Crystal packing of (a) **COSS**, (b) **CSSS** (AYOZAR), (c) **CSSS** polymorph (AYOZAR01) and (d) **CSSeS** (CCDC code: NABQUC), showing the presence of π-stacking, hydrogen bonding (cyan) and chalcogen bonding (purple) interactions.

The fourth carbonyl derivative, **COSSe**, crystallizes in the monoclinic system, space group *C*2/*c*, with one molecule in the asymmetric unit. It is isostructural with the two prepared thiocarbonyl derivatives **CSSS** and **CSSSe** [Figure S4-S6]. Note that the structure of **CSSS** has been already reported with two different polymorphs (CCDC codes: AYOZAR (space group *C*2/*c*)[50] and AYOZAR01 (space group $P2_1/n$)).[51] The overall crystal packing of these three-isostructural crystal structures **COSSe**, **CSSS** and **CSSSe** [Figure 2(b), Figures S4- S6] is very similar to that observed for the previous set of isostructural crystal structures (**COSS**, **COSeS** and **COSeSe**). Here, the molecular packing also consists of π-stacked molecules forming chains interlinked to each other *via* hydrogen and chalcogen bonding interactions. The difference in the molecular packing of this set of molecules is primarily because the molecule in the asymmetric unit forms π-stacking molecular chains using two alternating and unique π-stacking motifs (Table S3), which results in the formation of ····AAAAAAAA···· chains [Figure 2(b)], as opposed to ····AABBAABB···· chains in the previous set of molecules formed by two molecules (A and B) present in the asymmetric unit (Figure 2(a)]. In addition to the appearance of chalcogen bonding interactions, the presence of a chalcogen-chalcogen contact (involving Se at Ch3 position, see Table S4) similar to a type-I halogen-halogen interaction also shows in the crystal structures of **COSSe** and **CSSSe**.

For comparison purposes, we also describe hereafter the other crystal structures that, belonging to this series, were previously reported in the literature. They concern the second polymorph of **CSSS** and **CSSeS**. **CSSS** (AYOZAR01)[51] crystallizes in the monoclinic system, space group $P2_1/n$, with one molecule in the asymmetric unit. Only one unique π-stacking motif (molecular centroid-centroid distance = 4.006 Å) is observed, which results in the formation of ····AAAAA···· molecular chains running along the ***a***-axis [Figure 2(c)]. Similar π-stacked molecular chains are observed in a *zig-zag* arrangement down the ***c***-axis with interconnectivity provided by hydrogen and chalcogen bonding interactions [Figure 2(c), Table S5]. Down the ***b***-axis, the interconnectivity between closer parallel-arranged π-stacked chains is supported by hydrogen bonding interactions (Figure S7, Table S5).

CSSeS crystallizes in the monoclinic system, space group $P2_1/c$, with two molecules (A and B) in the asymmetric unit (CCDC code: NABQUC).[52] For the analysis of possible hydrogen bonding interactions, we have added hydrogen atoms at calculated positions as they were not reported in the original work. The main feature of this crystal structure concerns the presence of two similar chains of π-stacking molecules (Figure 2(d)), leading to ····AAAA···· and ····BBBB···· arrangements with very similar stacking distances (A···A = 4.100 Å, B···B = 4.100 Å). It is also interesting to note that **CSSeS** presents the largest number of chalcogen bonding interactions among all crystal structures analyzed in this study (Figure S8, Table S6).

Overall, it appears that the crystal packing of these chalcogen-rich aromatic molecules is primarily stabilized by π-stacking motifs, complemented with different hydrogen bonding and chalcogen bonding interactions that act as linkers for connecting the π-stacked molecular chains. With the aim of exploring the specific anchoring sites associated with the Ch2−Ch3 bond (S−S, S−Se, Se−Se), we will now focus exclusively on the chalcogen bonding interactions present in these structures.

*Chalcogen Bonding Interactions. 1. Effect of replacing sulfur with selenium in Ch2-Ch3 bond (**COSS** vs. **COSeSe**).* There exist three unique motifs in both **COSS** and **COSeSe** that can be described in terms of chalcogen bonding interactions (Figure 3, Table 1). Motif **I** consist of a double Ch2/Ch3•••O interaction (Ch = S, Se) bifurcated at O, which acts as a nucleophile, involving the R2 σ-hole region (see scheme 1 for localization of R1A, R1B and R2 σ-hole regions). This motif is further supported by the presence of an additional ChB interaction (Ch2•••Ch3), utilizing the R1A σ-hole region at Ch2. Hence, in motif **I**, in addition to the previous bifurcated interaction at O, a further double Ch3•••O/Ch2 interaction shows bifurcated

at Ch3, both sharing the Ch3•••O contact. The chalcogen atom present at Ch3 position in two of the molecules is involved in the formation of a Ch3•••Ch3 chalcogen bond interaction *via* the R1b σ-hole region (motif **II** in Figure 3). The Ch2 chalcogen atom also acts as a nucleophile, resulting in a possible double Ch2•••Ch2/Ch3 chalcogen bonding motif (bifurcated at Ch2) involving the R2 σ-hole region (motif **III** in Figure 3). The intermolecular distance between the chalcogen atoms in some of the possible chalcogen bonding interactions are large (reduction ratio RR > 1, Table 1), based on the vdW distance criteria.[53] The existence, strength and directionality of these bonding interactions will be further analyzed *via* the topological analyses of $\rho(\mathbf{r})$ and $L(\mathbf{r})$ in subsequent sections. Overall, it appears from the geometrical parameters (d, ζ_1, ζ_2 in Table 1) that all three possible σ-hole regions present around the Ch2-Ch3 bond are participating in the formation of directional chalcogen bonding interactions, the strongest ones seeming to involve the R2 region from the structural RR parameter. The chalcogen bonding network in **COSeS** (Figure S9, Table S7) is similar to that of **COSS** and **COSeSe** due to isostructurality.

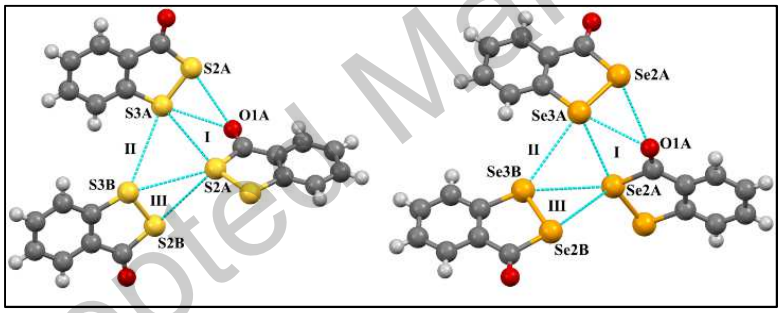

Figure 3. ChB motifs in **COSS** (left) and **COSeSe** (right). Labels A and B in the suffix of atomic symbols point the two molecules present in the asymmetric unit.

Table 1. Structural Characteristics of the ChB Interactions in **COSS** and **COSeSe**.*

Compound	Motif	Interaction	σ-hole	*d* (Å)	RR	ζ_1 (°)	ζ_2 (°)
COSS	I	C7A/S2A-S3A•••O1A=C1A	R2	3.081	0.93	165.1/74.0	114.6
		C1A/S3A-S2A•••O1A=C1A	R2	3.199	0.96	162.7/67.8	115.2
		C1A/S3A-S2A•••S3A-C7A/S2A	R1A	3.701	1.00	165.1/77.1	128.7/92.4
	II	C7A/S2A-S3A•••S3B-C7B/S2B	R1B	3.837	1.04	90.4/148.6	139.6/109.7
	III	C7B/S2B-S3B•••S2A-C1A/S3A	R2	3.830	1.03	162.1/78.9	123.3/131.0
		C1B/S3B-S2B•••S2A-C1A/S3A	R2	3.984	1.08	160.7/0.6	110.7/115.2
COSeSe	I	C7A/Se2A-Se3A•••O1A=C1A	R2	3.125	0.91	160.8/72.7	111.5
		C1A/Se3A-Se2A•••O1A=C1A	R2	3.292	0.96	155.8/64.9	113.1
		C1A/Se3A-Se2A•••Se3A-C7A/Se2A	R1A	3.596	0.95	78.5/165.8	125.5/93.4
	II	C7A/Se2A-Se3A•••Se3B-C7B/Se2B	R1B	3.819	1.00	88.5/147.1	143.1/103.1
	III	C7B/Se2B-Se3B•••Se2A-C1A/Se3A	R2	3.769	0.99	159.8/76.2	128.3/130.6
		C1B/Se3B-Se2B•••Se2A-C1A/Se3A	R2	3.925	1.03	157.7/68.8	110.9/112.9

**d* corresponds to the intermolecular distance between the atoms participating in the chalcogen bond interaction. RR is the reduction ratio, defined as the ratio between the intermolecular distance (*d*) and the sum of van der Waals radii of interacting atoms. ζ_1 and ζ_2 angles are defined in Figure 1.

*Chalcogen Bonding Interactions. 2. Effect of replacing carbonyl with thiocarbonyl (**COSS** vs. **CSSS**).* Replacing carbonyl with thio-carbonyl group results in notable changes in chalcogen bonding interactions, along with changes in molecular packing [*cf*. Figures 2(a) and 2(b)(c)]. In terms of ChB interactions, **CSSS** have two unique motifs in the AYOZAR polymorph, while only one appears in the AYOZAR01 polymorph (Figure 4, Table 2). Motif **I** in AYOZAR is actually similar to motif **I** observed in the crystal structure of **COSS** (and therefore also in the isostructural **COSeSe**) as it involves both regions R1A and R2 as ChB donors. Motif **II** in AYOZAR utilizes the R1B region in the formation of a chalcogen bonding interaction. The unique aspect of this motif is that the magnitude of the ζ_2 angle ($\angle$C=S…S) ~ 150° (Table 2) is much larger than expected for a usual *lone-pair* position of the sulfur atom. This chalcogen bonding network observed in **CSSS** AYOZAR polymorph is found identical in isostructural **COSSe** and **CSSSe** compounds (Figure S9, Table S7). On the other hand, the only ChB motif in the AYOZAR01 polymorph of **CSSS** (Figure 4 right) consists of a single interaction between the R2 σ-hole region with the *lone-pair* of thio-carbonyl sulfur atom.

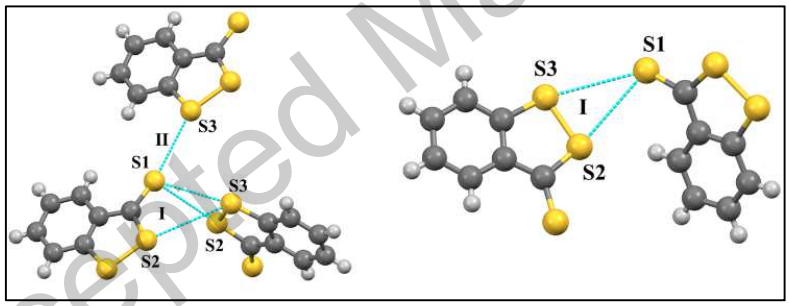

Figure 4. ChB motifs in AYOZAR (left) and AYOZAR01 (right) polymorphs of **CSSS**. The atomic labels used in this figure are different from the ones reported in the literature in order to be consistent with these across the molecules discussed in the manuscript.

Table 2. Structural Characteristics of the ChB Interactions in Both Polymorphs of **CSSS** (CCDC codes: AYOZAR and AYOZAR01).*

Compound	Motif	Interaction	σ-hole	*d* (Å)	RR	ζ_1 (°)	ζ_2 (°)
CSSS (AYOZAR)	I	C7/S2–S3•••S1=C1	R2	3.428	0.95	164.1/71.0	107.1
		C1/S3–S2•••S1=C1	R2	3.376	0.94	170.7/73.7	98.7
		C1/S3–S2•••S3-C7/S2	R1A	3.955	1.10	86.6/164.4	128.5/76.6
	II	C7/S2S3•••S1=C1	R1B	3.373	0.94	100.2/151.2	153.7
CSSS (AYOZAR01)	I	C7/S2–S3•••S1=C1	R2	3.555	0.99	163.1/71.6	127.8
		C1/S3–S2•••S1=C1	R2	3.503	0.97	167.4/74.4	95.9

* *d* corresponds to the distance between the atoms participating in the chalcogen bond interaction. RR is the reduction ratio, defined as the ratio between the intermolecular distance (*d*) and the sum of van der Waals radii of interacting atoms. ζ_1 and ζ_2 angles are defined in Figure 1.

Finally, the crystal structure of **CSSeS** has a unique network of chalcogen bonding interactions and is not isostructural with any other crystal structure of the analyzed family (see Figure S9 and Table S7).

In summary of this section, it appears that despite their closely related molecular structures, the solid-state organization of these compounds can vary significantly, particularly when considering which one of the possible σ-holes around the Ch2–Ch3 bond is actually engaged in a ChB interaction. On the other hand, the analysis of the geometrical parameters of the different chalcogen bonds present in the crystal structures shows that all three possible σ-hole regions are actually capable to participate in the formation of chalcogen bonding interactions, with the strongest ones involving the R2 σ-hole region as observed from the structural RR parameter.

Regions and Anchoring Sites for Molecular Assembly and Reactivity around the Ch2-Ch3 Bond in Monomers. In the following, we will first perform a thorough theoretical investigation of the electrostatic potential and the topological features of $\rho(\mathbf{r})$ and $L(\mathbf{r}) = -\nabla^2\rho(\mathbf{r})$, particularly around the dichalcogenide bond of individual molecules. This initial step will permit to determine the location of the most electrophilic chalcogen atoms within these series, as well as to give a rationale for understanding molecular assembly in the solid state and chemical reactivity.

Electrostatic Potential Maps. The presence of a σ-hole is often associated with the presence of a positive electrostatic potential region around the chalcogen atom.[54] Accordingly, DFT calculations of the electrostatic potential (ESP) have been performed for the eight compounds investigated in this study. For a better visualization of positive ESP regions around the Ch2–Ch3 dichalcogenide bond, maps have been drawn on the molecular ρ = 0.002 a.u. isosurface (Figure 5 and Figure S10). For comparison, ESP calculations mapped on the molecular ρ = 0.001 a.u. isosurface are gathered in Figures S11 and S12.

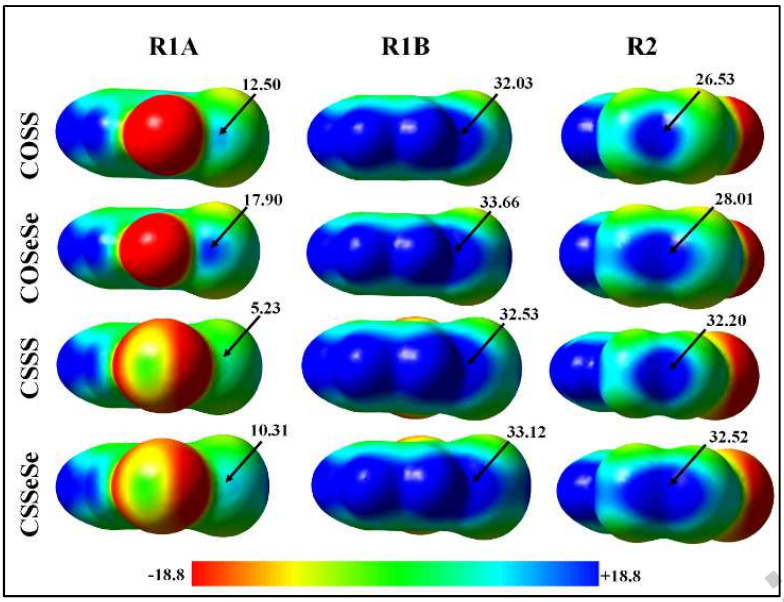

Figure 5: ESP maps of **COSS**, **COSeSe**, **CSSS** and **CSSeSe** drawn along R1A, R1B and R2A σ-hole regions. ESP is mapped on the molecular $\rho = 0.002$ a.u. isosurface. Blue: positive, Red: negative. ESP values in the figure are reported in kcal/mol. See Figure S10 for others compounds.

In region R1A, a relatively low magnitude of positive ESP is observed for the four compounds, with small larger magnitudes for selenium derivatives as compared to sulfur ones (Figure 5). The positive magnitude of ESP decreases when the thiocarbonyl group replaces the carbonyl group. The low magnitude of positive ESP in this region is due to the negative contribution of neighboring C=O/C=S groups. This trend can influence the σ-holes associated to chalcogen atoms, which can be significantly affected by neighboring atoms in the region of interest (namely, around the Ch2–Ch3 bond in our study). Accordingly, whereas we have already established the involvement of the R1A σ-hole region in chalcogen bonding formation (see the crystal structures described above), the ESP maps can be unable to disclose the true electrophilic character of the chalcogen atom along this R1A σ-hole region.

The positive magnitude of ESP in region R1B is found considerably higher than that observed in region R1A. Here, the ESP distribution is however significantly influenced by the positive contribution coming from the acidic hydrogen atom in the close vicinity, making difficult to assess the actual contribution of the chalcogen atom to the observed position and magnitude of the ESP maxima.

In region R2, while two σ-holes could be considered (each along the prolongation of one of the two C–Ch bonds), only one positive ESP extremum appears. It shows close to the

center of Ch2−Ch3 bond and results from the merged contribution of both chalcogen atoms. As a consequence, the magnitude of the positive ESP in this region is high, clearly establishing the presence of a unique σ-hole region caused by two contributions. This feature well corroborates with the formation of a short and directional chalcogen bonding interaction *via* this region. In addition, it is pointed out that the ESP magnitude in the R2 region is higher for molecules with the thiocarbonyl group than for those bearing the carbonyl group, and for those bearing Se instead of S at Ch2 and Ch3 positions.

Topology of $\rho(\mathbf{r})$. From the above ESP analysis, it is difficult to obtain an accurate description permitting to understand the electrophilic behavior of the chalcogen atoms in these molecules. Experimental and theoretical studies have clearly established that nucleophile attack on the chalcogen atoms Ch2 and Ch3 is possible along all the three possible σ-hole regions.[16,41] It is also well documented that the dichalcogenide Ch2−Ch3 bond is often considered as the weakest one within this family of molecules and is highly susceptible to follow up a nucleophilic attack.[16,55-61] In comparison to other covalent bonds in such 1,2-dichalcogenoles, the weak nature of Ch2−Ch3 can be established by QTAIM calculations performed on the optimized molecules in gas-phase. Indeed, as gathered in Table 3, which focuses on all the covalent bonds where chalcogen atoms are involved (for the rest of the bonds and molecules see Tables S8 and S9), the Ch2−Ch3 bond exhibits the lowest magnitudes of ρ and $\nabla^2\rho$ at BCP's. For Ch2−Ch3, while $|V|/G > 2$ and $\nabla^2\rho < 0$ establish unambiguously the covalent nature of the bond, its $|V|/G$ value is smaller than those observed for other bonds present in the molecules, except for C=Ch1 (C=O, C=S) that also possess a more negative $\nabla^2\rho$ magnitude and therefore a higher concentration of charge. The relatively low magnitude of $|V|/G$ for C=O and C=S can be attributed to the nature of these bonds that are highly polarized. The topological parameters of the S−S bond in **COSS** are similar to those observed in **CSSS**. Likewise, the topological parameters of the Se−Se bond in **COSeSe** are similar to those observed in **CSSeSe**. This suggests that replacing C=O by C=S does not significantly affect the electronic characteristics of the Ch2−Ch3 bond. In comparison, as expected, replacing sulfur by selenium (**COSS** *vs*. **COSeSe**, and **CSSS** *vs*. **CSSeSe**) leads to a notable weakening of the dichalcogenide bond, as shown by the recurrent lower magnitudes of ρ, $\nabla^2\rho$ and $|V|/G$ obtained for the Se−Se bond (Table 3).

Table 3. Topological Parameters of the Covalent Bonds Bearing Chalcogen Atoms in **COSS**, **COSeSe**, **CSSS** and **CSSeSe**.* See Tables S8and S9 for other compounds and bonds.

	COSS			**COSeSe**			**CSSS**			**CSSeSe**		
	ρ	$\nabla^2\rho$	|V|/G	ρ	$\nabla^2\rho$	|V|/G	ρ	$\nabla^2\rho$	|V|/G	ρ	$\nabla^2\rho$	|V|/G
Ch2–Ch3	0.95	-2.65	2.60	0.68	-0.82	2.26	0.93	-2.45	2.56	0.67	-0.72	2.23
Ch2–C1	1.20	-5.48	3.04	0.96	-2.53	2.53	1.38	-8.28	3.30	1.09	-3.47	2.55
Ch3–C7	1.35	-8.32	3.40	1.07	-3.39	2.56	1.36	-8.51	3.42	1.07	-3.48	2.57
Ch1–C1	2.89	-7.54	2.11	2.90	-6.15	2.09	1.53	-4.77	2.21	1.54	-5.18	2.23

* ρ is in e/Å^3, $\nabla^2\rho$ is in e/Å^5, |V|/G is dimensionless

To further analyze the characteristics of the chalcogen atoms, their net charges have been computed by integration within their atomic basins[38] and are collected in Table 4 for the eight compounds (see Table S10 for all atoms). The net charge of Ch3 remains unaffected when comparing a carbonyl-containing molecule with its thiocarbonyl counterpart. On the other hand, Ch2 becomes more positively charged from C=O to C=S derivatives (Table 4). The reason is brought close to the fact that, in case of thio-carbonyl derivatives, the *lone-pairs* of Ch2 are delocalized over the C1–Ch1 and C1–Ch2 bonds, resulting in a decrease of the electron population belonging to Ch2. This behavior is supported by the topological parameters associated with C1–Ch2 bonds (Table 3). Indeed, the C1–Ch2 bond is stronger in case of thio-carbonyl derivatives (larger magnitudes of ρ and |V|/G, and more negative $\nabla^2\rho$ value) as compared to its carbonyl containing counterpart. The net charge of atoms also reveals that the polarization of C=Ch1 changes, depending on the chalcogen atom. Thus, while the C=O bond exhibits the expected $\delta^+\ldots\delta^-$ character, the C=S bond shows surprisingly the opposite $\delta^-\ldots\delta^+$ polarization, further supporting the delocalization of Ch2 *lone-pairs* in the case of C=S. The larger net positive charge found for Ch2 is also consistent with the results obtained from the ESP analysis (Figure 5), which shows a larger positive ESP magnitude in region R2 for molecules bearing C=S instead of C=O. In carbonyl derivatives (Ch1 = O), the very high positive charge found for C1 might explain the specific reactivity of these compounds toward nucleophiles, leading to C1–Ch2 bond scission.[16] The same reactivity is also observed for **CSSS**,[28,29] but probably for a different reason as it is actually the Ch2 chalcogen atom that bears the highest positive charge.

Table 4. Integrated charges (in *e*) on selected atoms involved in chalcogen bonds.

	COSS	**COSSe**	**COSeS**	**COSeSe**	**CSSS**	**CSSSe**	**CSSeS**	**CSSeSe**
Ch1	-1.13	-1.13	-1.13	-1.13	0.14	0.14	0.16	0.16
Ch2	0.02	-0.08	0.20	0.09	0.15	0.05	0.35	0.24
Ch3	0.08	0.28	-0.03	0.17	0.08	0.27	-0.04	0.16
(Ch1=)C1	0.96	0.96	0.90	0.90	-0.46	-0.45	-0.55	-0.55
(Ch3–)C7	-0.16	-0.24	-0.15	-0.23	-0.16	-0.24	-0.15	-0.24

Topology of $L(\mathbf{r}) = -\nabla^2\rho(\mathbf{r})$. In order to further assess the electrophilic power of chalcogen atoms in the series, we have also analyzed the $L(\mathbf{r})$ function around the Ch2−Ch3 covalent bond (Figure 6 and Figures S13-S16). Previous studies on halogen and chalcogen bonding have clearly demonstrated the usefulness of $L(\mathbf{r})$ in describing the nucleophilic and electrophilic regions in the valence-shell of this kind of atoms.[10,43] In atomic basins, even when only the external valence-shell is considered, a large number of CPs derived from $L(\mathbf{r})$ are observed. For chalcogen atoms (Ch1, Ch2 and Ch3), nucleophilic charge concentration (CC) sites are well identified in their *lone-pairs* regions as (3,-3) CPs (Figure S13). These (3,-3) CPs (CC sites) appear by pairs with hybridized geometries at $Ch1_{sp2}$, $Ch2_{sp3}$ and $Ch3_{sp3}$ positions, in the molecular plane for Ch1, and in the planes bisecting the C-Ch2-Ch3 and C-Ch3-Ch2 angles for Ch2 and Ch3, where the *lone-pairs* of Ch1, Ch2 and Ch3 stand (Figure S13, Table S11-12). As expected, the nucleophilic power follows the trend O > S > Se (Table S11). The nucleophilic power of CC sites is slightly lower at Ch2 than at Ch3 for molecules with Ch2 = Ch3 (for example, in **COSS**, L/ρ = 9.2 and 9.7 $Å^{-2}$ respectively). These CPs are important because the location of other observed CPs are actually dictated by the location of dominant (3,-3) CPs. The potential electrophilic charge depletion (CD) sites should lye close to the molecular plane around the Ch2−Ch3 bond and a careful look in type and position of corresponding CPs should be taken (Figure 6 and Figures S14-S16). As shown in Figure 6, the *Valence Shell Charge Concentration* (VSCC) of S-atoms around the S−S bond in **COSS** (and similarly in **CSSS**, Figure S14) reveals the presence of two (3,+1) CPs in the topology of $L(\mathbf{r})$ (marked as CP1a and CP1b) in the region around the extension of the S−S bond. In **COSS**, CP1a and CP1b are present with ∠Ch3-Ch2-CP1a and ∠Ch2-Ch3-CP1b angles of 154.7° and 152.4°, respectively (Table S13). Two additional (3,+1) CPs (marked as CP2a and CP2b) are also present with ∠C1-Ch2-CP2a and ∠C7-Ch3-CP2b angles of 149.0° and 151.8° roughly along the two single C−S bonds of the molecule (Table S13). In addition, the VSCC region also reveals the presence of two (3, –1) CPs (marked as CP3a and CP3b) that are placed in the planes where *lone-pairs* stand, bisecting the ∠C−S−S angles. Therefore, each sulfur atom in **COSS** (and in the other molecules) is associated with three unique CPs (two (3,+1) and one (3, –1)) laying in the molecular plane within the VSCC region (Figure 6, Figures S14-S16). This trend is fully consistent with the topology of $L(\mathbf{r})$ previously described for the sulfur atom.[10] The iso-surface $\nabla^2\rho(\mathbf{r}) = 0$ around the sulfur atoms (Figure 6, top-right) shows holes in regions R1A and R1B, where the critical points CP1a and CP1b are sitting partially visible in the 3D map.

In contrast, other CPs are not visible, hidden by the iso-surface. The cavities around the R1A and R1B regions indicate that a potential nucleophilic attack will be more favorable along the S−S bond than along the C–S bonds (region R2). In region R2, it is however noteworthy the existence of another (3,+1) CP (CP4a) placed out of the iso-surface $\nabla^2\rho(\mathbf{r}) = 0$ (in the atomic *Valence Shell Charge Depletion* region, VSCD), facing the S−S BCP. Figure 6 and the angular values ∠C1-Ch2-CP4a = 129.9° and ∠C7-Ch3-CP4a = 127.1° (similar to each other) clearly indicate that CP4a is very close to the interatomic Ch2-Ch3 surface, rather than along to the extension of C-Ch bonds. The emergence of this (3,+1) CP is the consequence of two (3,+3) CPs (CP4b and CP4c) in the closer neighborhood, making the region where the three CPs stand of significant electrophilic nature. As for CP1a (region R1A) and CP1b (region R1B), CP4a (region R2) also stands in the region of the expected σ-hole, as observed in the electrostatic potential maps (Figure 5). Hence, although the nucleophilic attack is more difficult through region R2 in the absence of a hole in the iso-surface $\nabla^2\rho(\mathbf{r}) = 0$, an electrostatic interaction can take place with the intermolecular environment involving this favorable electrophilic region, similarly to R1A and R1B. Finally, in the outer VSCD region of sulfur atoms another (3,+1) and (3,+3) CPs exhibit (namely, CP3c-f). They are placed in the molecular plane, and close to the planes bisecting the <C−S−S angles that contain the lone pairs of sulfur atoms. Consequently, although they are standing in regions with relevant electrophilic power (see their L/ρ values), they are less performant as anchoring sites for molecular assemblies, as eventual nucleophilic centers will feel the repulsion exerted by the lone-pairs that are in close vicinity. Furthermore, as CP4a-c sites, they are also out of the $\nabla^2\rho(\mathbf{r}) = 0$ isosurface, which is closed in this region and avoids the nucleophilic attack for reactivity purposes.

The descriptor L/ρ (Table 5 and Table S14) was computed in order to evaluate the electrophilic power of these sites. The lower is L/ρ the more important is the electrophilic power, because the electron distribution per charge density unit is more depleted. Whereas (3,+3) and (3,+1) CPs exhibit negative (or low positive) L/ρ magnitudes, (3,-1) CPs show large positive ones, clearly pointing the former as more efficient electrophilic sites. Around the S−S bond in **COSS**, the (3,+3) and (3,+1) CPs characteristic of regions R1a, R1b and R2 (namely, CP1a, CP1b and CP4a-c) exhibit the highest electrophilic power $-6.6 < L/\rho < 0$ Å^{-2}. It should be noted that, in spite of their topological features, CP2a-b and CP3a-b sites of S-atoms should be considered as bad electrophilic sites, as they show large $L/\rho > 0$. They are however included in the Table 5 for comparison purposes with the rest of CD sites.

For the corresponding diselenide **COSeSe**, all CPs are present in the outer Valence Sell Charge Depletion (VSCD) region, because the valence shell of the atom is fully depleted ($\nabla^2\rho(\mathbf{r}) > 0$) due to the screening made by the large quantity of core electrons in selenium atoms (Figure 5 bottom and Figures S14-S16). Around the Se−Se bond in **COSeSe**, and compared with the S−S bond in **COSS**, only (3,+1) CPs at CP1a, CP1b, CP3c, CP3d and CP4a sites, and (3,-1) CPs at CP3a and CP3b sites appear, the other CPs observed with S-atoms being merged by coalescence into one of the observed CPs in the same region with Se-atoms. The positions of CP1a/CP1b sites around selenium atoms are quite different with respect to these found around sulfur atoms. Indeed, while in **COSeSe** the angles ∠Ch3-Ch2-CP1a and ∠Ch2-Ch3-CP1b are both 129° (Table S13), in **COSS** they show at ~ 150°. Accordingly, CP1a and CP1b are found well into the basins of sulfur atoms in the disulfide, whereas in the diselenide they are close to the interatomic surfaces between carbon and selenium atoms, facing the C−Se BCPs (Figure 6). Hence, due to steric hindrance, CP1a and CP1b sites in selenium atoms can be less performant to generate directional intermolecular motifs along internuclear directions (low angle between CD…CC and internuclear directions) in the assembly of molecules. On the other hand, concomitantly to the shifting of CP1A and CP1b sites with respect to sulfur atoms, the selenium *lone-pairs* (*lp*'s) open their disposition (angles 144.8° < CC_{lp1}−Se_{sp3}−CC_{lp2}< 150°, 127.1° < CC_{lp1}−S_{sp3}−CC_{lp2}< 134.5 ° for all molecules) (Table S12), as previously observed with sulfur and selenium chalcogenophtalic derivatives.[10] This electronic feature permits an easier approach of nucleophiles along the direction bisecting the <C−Se−Se angles than along that of <C−S−S angles. CP3c and CP3d rank better than CP3a and CP3b in terms of preferred electrophilic sites in their respective regions, as shown by the more negative L/ρ values for the former (Table 5). This trend follows the general consideration that the electrophilic power of (3,+1) CPs is more important than that of (3, –1) CPs because $\rho(\mathbf{r})$ is depleted along two main directions for the former and along only one for the latter. As in the case of the S−S bond in **COSS**, an additional (3,+1) CP is here observed close to the center of the Se−Se bond (marked as CP4a), showing angles of ∠C1-Ch2-CP4a = 124.1° and ∠C7-Ch3-CP4a = 122.1° and with a significant electrophilic power that is even larger than this observed for CP3c and CP3d (see Table 5). However, as for CP1a/CP1b, CP4a shows close to the interatomic surface Se−Se and the corresponding BCP, where $\rho(\mathbf{r})$ is locally concentrated ($\nabla^2\rho(\mathbf{r}) < 0$). This makes more difficult a nucleophilic attack, even if this site can play a significant role in the molecular assembly, as steric hindrance does not take place as for CP1a/CP1b. As expected, the electrophilic power associated with CD sites around selenium atoms (–7.9 < L/ρ < –2.4 $Å^{-2}$) is

in general larger than with those of sulfur atoms (–6.9 < L/ρ < 0 Å^{-2}), even if for CP3c-d and CP4a slightly more negative values are found for S-atoms (Table 5).

Very similar trends to those found for CD sites belonging to S-atoms in **COSS** and to Se-atoms in **COSeSe**, are also observed for the same atoms in the other molecules of the same series (Figure S14-16 and Table S14). Indeed, the same CP types are closely placed in the same region of each atom type (S or Se) from one derivative to another, while the corresponding L/ρ values only vary in minor way. In addition, it is noteworthy that the pairs of (3,+1) CPs (CP1a/CP1b and CP3c/CP3f), as well as the pair of (3,-1) and (3,+3) CPs (CP3a and CP3e) observed in **COSS**, were formerly identified in the valence-shell of the S-atom in the sulfur derivative of a series of chalcogenophtalic molecules ($C_8O_2H_4Chal$, Chal = O, S, Se, Te).[10] In both families of molecules CPs are sitting at very similar positions. In what it concerns the Se-atom, the selenophtalic derivative showed the same pairs of CPs than those found around the S-atom in the thiophtalic derivative, whereas in the actual series the merge of sites by coalescence of CPs lead to a single CP per pair. For S- and Se-atoms, the observed L/ρ values in the corresponding CPs are more negative for CP1a/CP1b in the actual series than in the chalcogenophtalic derivatives (by ~ -1 to -2 Å^{-2}), remaining closely similar for the rest of CPs from one family to the other. Hence, whereas under the influence of a different intramolecular environment the topological features in the valence shell of atoms are globally conserved, the particular electronic properties found in the close neighborhood can modify in some measure their characteristics. With this respect, it should be also noted the different level of calculations (MP2 *vs* B3LYP) and basis sets used with each family of molecules. Consequently, the merged CPs found for selenium and the more powerful electrophilic sites found for both S- and Se-atoms at CP1a/CP1b sites are brought close to the increased electrophilic power of chalcogen atoms when they are embedded in Ch–Ch bonds.

Overall, the topological analysis of $L(\mathbf{r})$, pointing the relevant atomic sites on the electrophilic regions associated with the Ch2–Ch3 bond, gives a much more descriptive information than ESP maps. It confirms for example that CD sites prone to drive a potential nucleophilic attack on disulfides will be more favorable along the S–S bond in regions R1A and R1B, where the reactivity surface ($\nabla^2\rho(\mathbf{r}) = 0$) exhibits a hole. For Se-atoms, the contracted $\nabla^2\rho(\mathbf{r}) = 0$ isosurface in their valence shell indicates large accessible regions for nucleophilic attack in regions R1a and R1b. In molecular assemblies involving S-atoms, the pair of CD sites CP1a/CP1b show accessible in regions R1A/R1B for CD…CC interactions along the Ch2–Ch3 bond, whereas their position in Se-atoms made them less well placed due to their proximity to

the basin of the carbon atom, which can lead to steric hindrance. On the other hand, for both S- and Se-atoms, CD sites in region R2 (mainly CP4 sites) stand for a side-on intermolecular interaction of the Ch2–Ch3 bond with a nucleophile. For all derivatives in this study, as determined from the L/ρ values, the electrophilic power of CD sites in regions R1A and R1B of Se-atoms is significantly stronger than around S-atoms, whereas in region R2 it is slightly stronger around S-atoms.

Table 5. Electrophilic Power (L/ρ in $Å^{-2}$) of Charge Depletion (CD) Sites in the Electron Valence Shell of Chalcogen Atoms in Gas Phase. ρ and $\nabla^2\rho$ are in $e/Å^3$ and $e/Å^5$ units. See Table S14 for other compounds.

	Type	**COSS**			**COSeSe**			**CSSS**			**CSSeSe**		
		$\nabla^2\rho$	ρ	L/ρ	$\nabla^2\rho$	ρ	L/ρ	$\nabla^2\rho$	ρ	L/ρ	$\nabla^2\rho$	ρ	L/ρ
CP1a	(3,+1)	0.01	0.80	-0.01	2.69	0.34	-7.92	0.78	0.78	-1.00	3.02	0.39	-7.74
CP1b	(3,+1)	0.25	0.80	-0.31	2.68	0.36	-7.44	-0.03	0.82	0.04	2.67	0.36	-6.58
CP2a	(3,+1)	-1.86	0.88	2.11				-1.34	0.86	1.56			
CP2b	(3,+1)	-1.35	0.86	1.57				-1.60	0.87	1.84			
CP3a	(3,-1)	-8.68	1.16	7.48	1.38	0.59	-2.39	-9.27	1.19	7.79	1.29	0.62	-2.08
CP3b	(3,-1)	-8.29	1.15	7.21	1.47	0.57	-2.58	-8.26	1.15	7.18	1.45	0.57	-2.54
CP3c	(3,+1)	1.66	0.33	-5.03	1.58	0.36	-4.39	1.65	0.33	-5.00	1.55	0.35	-4.33
CP3d	(3,+1)	1.65	0.32	-5.16	1.58	0.37	-4.27	1.64	0.32	-5.12	1.56	0.36	-4.33
CP3e	(3,+3)	1.66	0.34	-4.88				1.67	0.34	-4.91			
CP3f	(3,+1)	1.63	0.33	-4.93				1.67	0.33	-5.06			
CP4a	(3,+1)	2.40	0.37	-6.49	1.56	0.29	-5.38	2.41	0.37	-6.51	1.55	0.29	-5.34
CP4b	(3,+3)	2.45	0.38	-6.45				2.55	0.38	-6.71			
CP4c	(3,+3)	2.52	0.38	-6.63				2.49	0.37	-6.73			

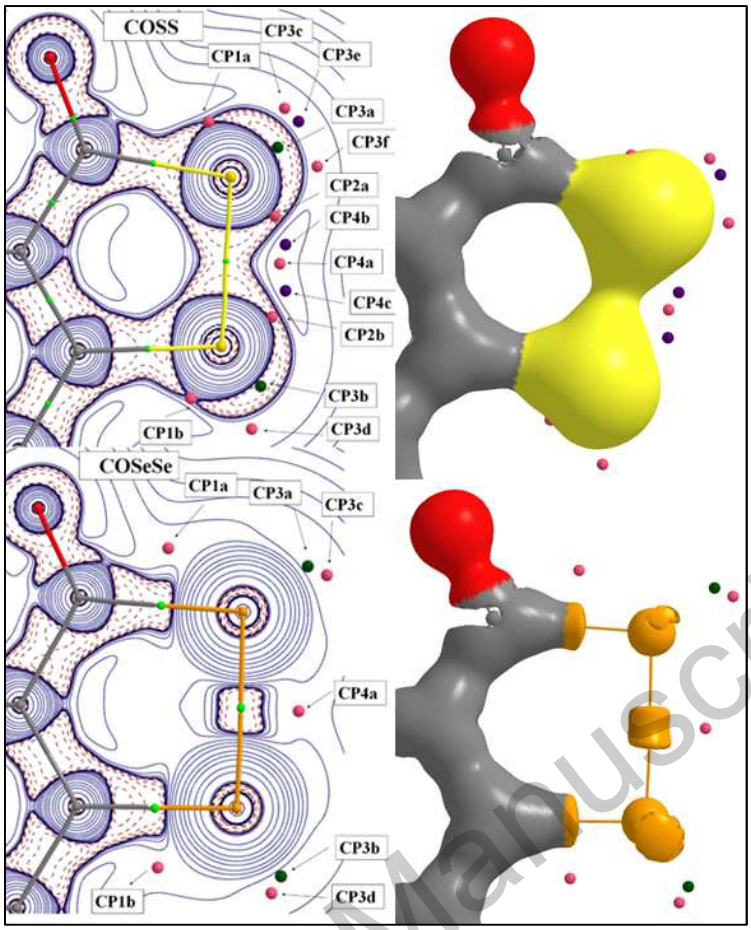

Figure 6. Left: $L(\mathbf{r}) = -\nabla^2\rho(\mathbf{r})$ maps [e/Å^5, contours are in logarithmic scale: positive (red) and negative (blue)] for **COSS** (top) and **COSeSe** (bottom). Right: The $\nabla^2\rho(\mathbf{r}) = 0$ maps are plotted for **COSS** (top) and **COSeSe** (bottom) with atomic portioning. Relevant CPs of $L(\boldsymbol{r})$ in the valence shell of chalcogen atoms are denoted in maps as spheres [(3, −1) CPs are green, (3, +1) CPs are pink and (3, +3) CPs are violet]. (3,-3) CPs corresponding to *lone-pairs* of Ch2 and Ch3 are out of plane in the left (they are shown in Figure S13), and hidden by the enclosing surfaces $\nabla^2\rho(\mathbf{r}) = 0$ in the right. See Figures S14–S16 for other compounds.

Anchoring Sites around the Ch2-Ch3 Bond for Molecular Assemblies. Following the above description of the electron density distribution in isolated molecules, particularly around the dichalcogenide bond, we now concentrate on its consequences on the organization of the molecules in space, with particular emphasis on the chalcogen bonding interactions identified in the crystal structures. For this purpose, we have carried out single-point calculations on dimers (and a trimer) extracted from the crystal structures.

1. Topology of $\rho(\boldsymbol{r})$. The involvement of all three possible σ-hole regions in the formation of chalcogen bonds (ChB) is indeed supported by the existence of bond critical points (BCPs) between the interacting atoms of neighboring molecules in the focused motifs (Figure 7-8, S17-S23). BCPs were also observed for several (not all) of the ChB interactions with intermolecular distances well beyond the sum of vdW radii. The magnitude of ρ at BCP ranges from 0.029 e/Å^3 to 0.082 e/Å^3 (Table 6, Table S15). All the interactions are of *pure* closed-shell interaction type with low positive values of $\nabla^2\rho$ and $|V|/G < 1$. The magnitudes of ρ and $\nabla^2\rho$ at BCPs are larger for Ch•••O interactions (Ch = S or Se) than for the other chalcogen bonding interactions present in the motifs. This feature can be attributed to the more important nucleophilic power of oxygen compared to other chalcogen atoms (see $(L/\rho)_{CC}$ values in Table S11).[10] It is important to note that BCPs are not observed for some contacts in motifs with multiple chalcogen bonding (ChB) interactions. These ChBs are mainly those showing a large reduction ratio value (RR > 1, see Table 6) and/or less linear chalcogen bonding interactions. For comparison, we have also determined the topological parameters for the trimer assembled by ChB interactions in **COSS** (see Figure 3) at the same level of theory. Compared to the dimers embedded in the trimer, a decrease is observed for the |V|/G ratio of ChBs in motif III (bonding interactions with large intermolecular distances), whereas no significant variation is observed for the magnitudes of ρ, $\nabla^2\rho$ and |V|/G in the rest of motifs (Table 6, Figure S23).

Table 6. Structural and topological characteristics of the ChB interactions obtained from dimers at crystalline geometries in **COSS** and **COSeSe**. Most relevant CD···CC interactions (see text) are in bold. Units are: d(Å), $d_{CC...CD}$(Å), α(°), ρ(e/Å^3), $\nabla^2\rho$(e/Å^5), L/ρ(Å^{-2}), $\Delta(L/\rho)$(Å^{-2}), $\Delta(L/\rho)/d^2_{CC...CD}$ (Å^{-4}) and |V|/G (dimensionless). See Table S15 for other compounds.

Compound	Motif	Interaction	σ-hole	*d*	*ρ*	RR	$\nabla^2\rho$	|V|/G	CD	$(L/\rho)_{CC}$	$(L/\rho)_{CD}$	$\Delta(L/\rho)$	$d_{CC...CD}$	$\Delta(L/\rho)/d^2_{CC...CD}$	*α*(°)
COSS	**I**	S3A•••O1A	R2	3.081	0.067 *0.067*	0.93	0.88 *0.88*	0.77 *0.77*	CP2a/ CP2b/	**16.24** ***(16.25)***	1.89 *(1.89)*	14.35 *(14.35)*	2.31 *(2.31)*	2.13 *(2.13)*	2.6 *(2.6)*
		S2A•••O1A	R2	3.199	-	0.96	-	-	CP3c/ CP3d/ **CP4a/** **CP4b/** **CP4c**		1.28 *(1.30)* -5.01 *(-5.02)*/ -5.07 *(-5.12)*/ **-6.81** ***(-6.82)***/ **-6.84** ***(-6.85)***/ **-7.13** ***(-7.14)***	14.96 *(14.94)* 21.25 *(21.27)*/ 21.31 *(21.37)*/ **23.05** ***(23.07)***/ **23.08** ***(23.10)***/ **23.37** ***(23.39)***	2.09 *(2.09)* 3.13 *(3.13)*/ 2.81 *(2.80)*/ **2.04** ***(2.04)***/ **2.04** ***(2.04)***/ **1.93** ***(1.93)***	3.42 *(3.42)* 2.17 *(2.17)* 2.70 *(2.72)* **5.54** ***(5.54)*** **5.54** ***(5.55)*** **6.27** ***(6.28)***	8.5 *(8.5)* 25.6 *(25.6)*/ 20.6 *(20.6)*/ **7.7** ***(7.7)***/ **12.9** ***(12.6)***/ **2.6** ***(2.6)***
		S2A•••S3A	R1A	0.39 *0.40*	0.69 *0.69*	1.00			**CP1a/** **CP3c**	**9.76** ***(9.76)***	**-0.13** ***(-0.12)***/ **-4.92** ***(-5.05)***	**9.89** ***(9.88)***/ **14.68** ***(14.81)***	**2.47** ***(2.47)***/ **3.11** ***(2.31)***	**1.62** **(1.62)** **1.52** ***(2.77)***	**12.9** ***(13.1)***/ **15.0** ***(11.2)***
	II	S3A•••S3B	R1B	3.837	0.031 *0.031*	1.04	0.32 *0.32*	0.67 *0.68*	**CP1b/** **CP3d**	**9.75** ***(9.74)***	**-0.38** ***(-0.41)***/ **-5.14** ***(-5.14)***	**10.13** ***(10.15)***/ **14.89** ***(14.86)***	**2.77** ***(2.77)***/ **2.44** ***(2.44)***	**1.32** **(1.33)** **2.50** ***(2.49)***	**5.7** ***(5.7)***/ **11.8** ***(11.5)***

	III	S3B•••S2A	R2	3.830	0.029 *0.028*	1.03	0.28 *0.32*	0.77 *0.70*	[CP2a/ CP2b/	**8.59** **(*9.19*)**	[2.38/ 2.11/	[6.21/ 6.48/	[2.71/ 2.71/	[0.84/ 0.88/	[10.3/ 5.7/
		S2B•••S2A	R2	3.984	0.026 *0.024*	1.08	0.24 *0.27*	0.81 *0.64*	CP3c/ CP3d/	**(CC1)**	-6.52/ -6.52/	17.18/ 15.11/	2.98/ 3.31/	1.93/ 1.38/	17.4/ 28.0/
									CP4a]#		**-8.59**] #	**15.11**]#	**2.50**]#	**2.42**]#	**8.1**]#
									[CP2a/ CP2b/ CP3c/ CP3d/ **CP4a/** **CP4b/** **CP4c**]##		[*1.99/* *1.46/* *-5.03/* *-5.14/* ***-6.53/*** ***-6.57/*** ***-6.80***] *##*	[*7.20/* *7.73/* *14.22/* *14.33/* ***15.72/*** ***15.76/*** ***15.99***] *##*	[*2.68/* *2.67/* *3.48/* *3.21/* ***2.52/*** ***2.49/*** ***3.24***] *##*	[*1.00/* *1.08/* *1.17/* *1.39/* ***2.47/*** ***2.54/*** ***1.52***] *##*	[*8.9/* *5.7/* *26.1/* *16.9/* ***6.8/*** ***4.4/*** ***8.9***] *##*
									CP2b/ CP3d	8.59 (*9.18*) (CC2)	2.11 (*1.46*) -6.52 (*-5.14*)	6.48 (7.72) 15.11 (*14.32*)	3.35 *(3.31)/* 3.45 *(3.64)*	0.58 *(0.70)/* 1.27 (*1.08*)	17.2 *(17.3)/* 6.8 *(6.3)*
COSeSe	**I**	Se3A•••O1A	R2	3.125	0.071	0.91	0.85	0.81	**CP4a/** CP3d	**16.30**	**-5.74/** -4.32	**22.03/** 20.61	**2.02/** 2.88	**5.40** **2.48**	**7.2/** 20.6
		Se2A•••O1A	R2	3.292	-	0.96	-	-	**CP4a/** CP3c	**16.30**	**-5.74/** -4.39	**22.03/** 20.68	**2.02/** 3.21	**5.40** 2.00	**7.2/** 25.2
		Se2A•••Se3A	R1A	3.596	0.065	0.95	0.52	0.87	**CP1a/** **CP3c**	**0.65**	**-8.02/** **-4.32**	**8.67/** **4.97**	**2.70** **2.25**	**1.19** **0.98**	**15.6/** **15.6**
	II	Se3A•••Se3B	R1B	3.819	0.045	1.00	0.38	0.81	**CP1b/** **CP3d**	**0.67**	**-7.54/** **-4.38**	**8.21/** **5.05**	**2.62/** **2.42**	**1.20** **0.86**	**3.6/** **16.6**
	III	Se3B•••Se2A	R2	3.769	0.043	0.99	0.42	0.78	**CP3c/**	**0.15**	**-4.39/**	**4.54/**	**2.82/**	**0.57**	**16.4/**
		Se2B•••Se2A	R2	3.925	0.039	1.03	0.36	0.76	CP3d/ **CP4a**	**(CC1)**	-4.32/ **-5.49**	4.47/ **5.64**	3.50/ **2.27**	0.36 **1.09**	30.5/ **12.0**
									CP3d	0.11 (CC2)	-4.32	4.43	3.68	0.33	2.6
CSSS (AYOZAR)	**I**	S3•••S1	R2	3.428	0.071	0.95	0.73	0.82	CP2a/ CP2b/	**9.17**	1.29/ 1.48/	7.88/ 7.69/	2.26/ 2.08/	1.54 1.78	7.3/ 9.2/
		S2•••S1	R2	3.376	0.074	0.94	0.75	0.84	CP3c/ CP3d/ **CP4a/** **CP4b/** **CP4c**		-5.09/ -5.05/ **-6.99/** **-7.17/** **-7.08**	14.26/ 14.22/ **16.16/** **16.34/** **16.25**	3.13/ 2.90/ **2.00/** **2.01/** **1.93**	1.45 1.69 **4.04** **4.04** **4.36**	30.7/ 18.6/ **9.2/** **17.6/** **3.6**
		S2•••S3	R1A	3.955	-	1.10	-	-	**CP1a** **CP3c**	**9.57**	**-1.0/** **-5.13**	**10.57** **14.7**	**2.87** **2.44**	**1.28** **2.47**	**14.5** **2.6**
	II	S3•••S1	R1B	3.373	0.065	0.94	0.72	0.78	**CP1b/** CP3d	**8.92** **(CC1)**	**-0.02** -5.30	**8.94/** 14.22	**2.79** 2.42	**1.15** 2.43	**6.3** 21.3
									CP1b/ **CP3d**	**9.18** **(CC2)**	-0.02 **-5.30**	9.20/ **14.48**	2.93/ **2.28**	1.07 **2.78**	24.2/ **19.8**
CSSS (AYOZAR01)	**I**	S3•••S1	R2	3.555	-	0.99	-	-	CP2a/ CP2b/	**8.89**	1.30/ 1.57/	7.59/ 7.32/	2.38/ 2.49/	1.34 1.18	11.5/ 9.2/
		S2•••S1	R2	3.503	0.060	0.97	0.60	0.79	CP3c/ **CP4a/** **CP4b/** **CP4c**		-5.08/ **-6.90/** **-7.12/** **-6.98**	13.97/ **15.79/** **16.01/** **15.87**	2.98/ **2.28/** **2.21/** **2.26**	1.57 **3.04** **3.28** **3.10**	21.9/ **11.5/** **9.9/** **15.0**

* α is the angle between Ch…Ch and CC…CD directions, except for CP1a-b (for Se) and CP4a-c sites for which α is calculated between Ch…BCP and CC…CD directions (see text). Italic values everywhere correspond to values obtained in the trimer of **COSS**. Symbols [#] and [##] read for CD sites obtained in motif **III** of dimer (denoted by #) and trimer (denoted by ##). Their topological features are very similar in motifs **I** and **II**, and only slightly different in motif **III**, where the CP4a-c sites in the trimer merge in only one CP4a (3,+3) site in the dimer.

2. *Topology of* $L(\mathbf{r}) = -\nabla^2\rho(\mathbf{r})$. In the intermolecular regions where ChB show, the position of CP's derived from the $L(\mathbf{r})$ function indicates that local nucleophilic···electrophilic interactions take place *via* a face-to-face orientation of a (3,−3) CP acting as a CC site and a (3,+1) CP (or a (3,+3) CP in few cases) acting as a CD site (Figures 7-8, Figures S17-S23). This trend follows the general consideration that (3,-1) CPs cannot compete with (3,+1) CPs if they are present in adjacent positions, because of the more powerful electrophilic character of the latter. When several (3,+1) CPs appear in the same region, it is likely expected that all of them will be involved in the interaction with the nucleophilic center. For sulfur, CP1a/CP3c along region R1A, CP1b/CP3d along region R1B, and CP2a-b/CP4a-c/CP3c-d in region R2 emerge as possible CD sites involved as electrophiles. For selenium, CP1a/CP3c along region R1A, CP1b/CP3d along region R1B, and CP4a/CP3c-d in regions R2 emerge as the possible CD sites

involved as electrophiles. In all the interactions, (3,-3) CPs were involved as nucleophilic sites. The local electrostatic intensity of the electrophilic···nucleophilic interactions was evaluated using the normalized quantity $\Delta(L/\rho) = (L/\rho)_{CC} - (L/\rho)_{CD}$, its magnitude varying in the range $1.1 < \Delta(L/\rho) < 23.9$ Å^{-2} for all the reported CC···CD interactions in the crystal structures (excluding three negative $\Delta(L/\rho)$ values in **COSeS** and **CSSeS**, see Table S15). From Table 6, larger $\Delta(L/\rho)$ magnitudes correspond to shorter $d_{CC}\cdots d_{CD}$ distances, indicating that more powerful electrophilic···nucleophilic interactions lead to shorter CC···CD geometries, and therefore to stronger driving forces in the assembling of molecules. Strikingly, the angle α between CC···CD and Ch···Ch' (Ch = S, Se; Ch' = O, S) directions is less than ~15° for stronger electrophilic···nucleophilic interactions ($\Delta(L/\rho) > \sim 5$ Å^{-2}, see Tables 6 and S15), which also corresponds to shorter CC···CD distances ($d_{CC\cdots CD} < \sim 2.7$ Å). As reported in previous studies,[10,43] low magnitudes of α (< ~15°) point for local electrostatic electrophilic···nucleophilic (CD···CC) interactions that are at the origin of geometrical preferences in molecular assemblies, as a consequence of their ability to impose the relative orientation of interatomic interactions (Ch···Ch' in this work). Note that less performant CD sites show larger α-angles (> ~20°) and $d_{CC\cdots CD}$ distances (> ~2.9 Å), in spite to exhibit sometimes non-negligible $(L/\rho)_{CD}$ values (see, for instance, CP3d sites in Table 6). Consequently, they will lead to weaker electrophilic…nucleophilic interactions than other CD sites in the close vicinity, which usually show larger $(L/\rho)_{CD}$ values and significantly lower α and $d_{CC\cdots CD}$ magnitudes (in Table 6**,** see for instance the contributions of CP3d and CP4a sites in the Se2A•••O1A and Se2B•••Se2A interactions of **COSeSe**). With the aim to analyze the intensity of the electrophilic…nucleophilic interaction with a unique descriptor, we introduce the magnitude $\Delta(L/\rho)/d^2_{CC\cdots CD} = [(L/\rho)_{CC} - (L/\rho)_{CD}]/d^2_{CC\cdots CD}$ (see section 2.2), which increases with the electrophilic and the nucleophilic power of the sites and with shorter distances, and permits to identify most relevant interactions. Therefore, the larger is the positive value of $\Delta(L/\rho)/d^2_{CC\cdots CD}$ the larger is the intensity of the interaction (0.09 Å$^{-4} < \Delta(L/\rho)/d^2_{CC\cdots CD} < 7.47$ Å^{-4} for the CC…CD interactions in this work, excluding three negative values). This is particularly interesting to focus on relevant CC···CD interactions when several of them are occurring simultaneously in a region of the intermolecular space. Hence, the descriptor has been used to select relevant interactions in Table 6 and in Figures 7 and 8 (for the rest of interactions see Table S15 and Figures S17-S23 in S.I.).

It is important to point out that the electrophilic region where CP4a-c sites show, rises as the simultaneous contribution of both chalcogen atoms. Consequently, for calculating the α-

angle magnitude that involves these CD sites, the reference point is neither Ch2 nor Ch3 nuclear coordinate but the Ch2-Ch3 BCP. Similarly, in the case of selenium atoms, CP1a and CP1b sites are observed very close to the C-Se interatomic surface, shifting their positions towards the corresponding BCP. Hence, as for CP4a-c in Ch2-Ch3, the α-angle corresponding to CP1a and CP1b sites of Se-atoms is calculated taking the BCP as reference point instead of the Se-nuclear coordinate. This choice is in line with the previous ESP observations, where the local maxima of the electrophilic regions R1A, R1B and R2 emerged shifted towards the middle of C-Ch2, C-Ch3 and Ch2-Ch3 bonds.

Consistent with previous studies, the Se•••O chalcogen bonding interaction exhibits the largest electrophilic•••nucleophilic intensity, followed by the S•••O interaction, as described from their $\Delta(L/\rho)/d^2_{CD\cdots CC}$ magnitudes. It should be pointed out that these strongest electrostatically driven Se•••O and S•••O interactions involve the σ-hole in region R2 because of its significant electrophilic character, while it is sterically more favorable for the nucleophile (namely, the carbonyl oxygen) to interact through this region.

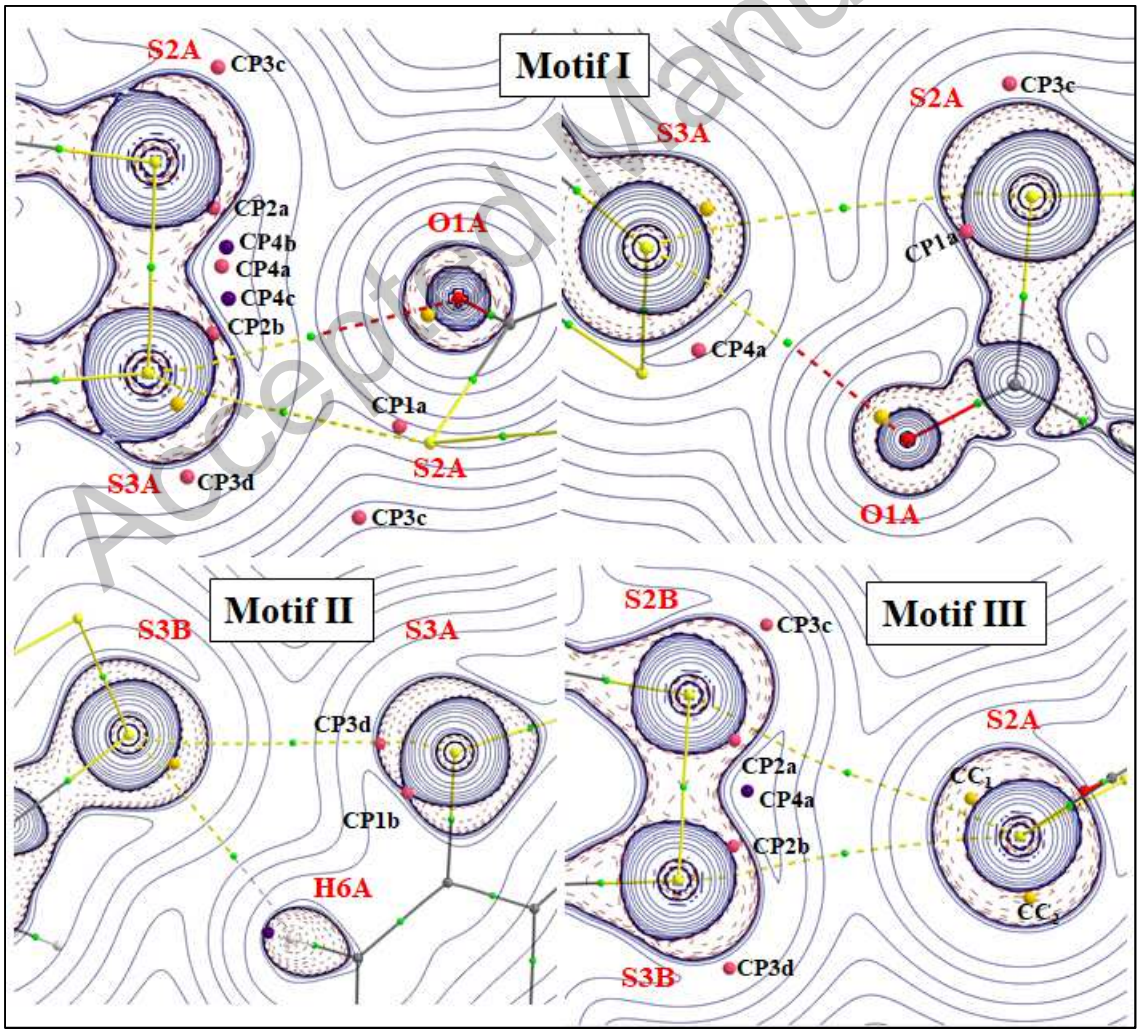

Figure 7. Intermolecular bond critical points (BCPs, small green spheres), intermolecular bond paths (dashed lines) and charge concentration and charge depletion (CC/CD) sites (yellow/pink/violet spheres) involved in the chalcogen bonding interactions present in motifs **I**, **II** and **III** of **COSS**, as well as a hydrogen bonding interaction in motif **II**. CPs of $L(\mathbf{r})$ are: (3,−3) in yellow , (3+1) in pink, (3,+3) in violet. Most relevant CD/CC sites are indicated in bold in Table 6 and show close to the molecular planes represented in the figures.

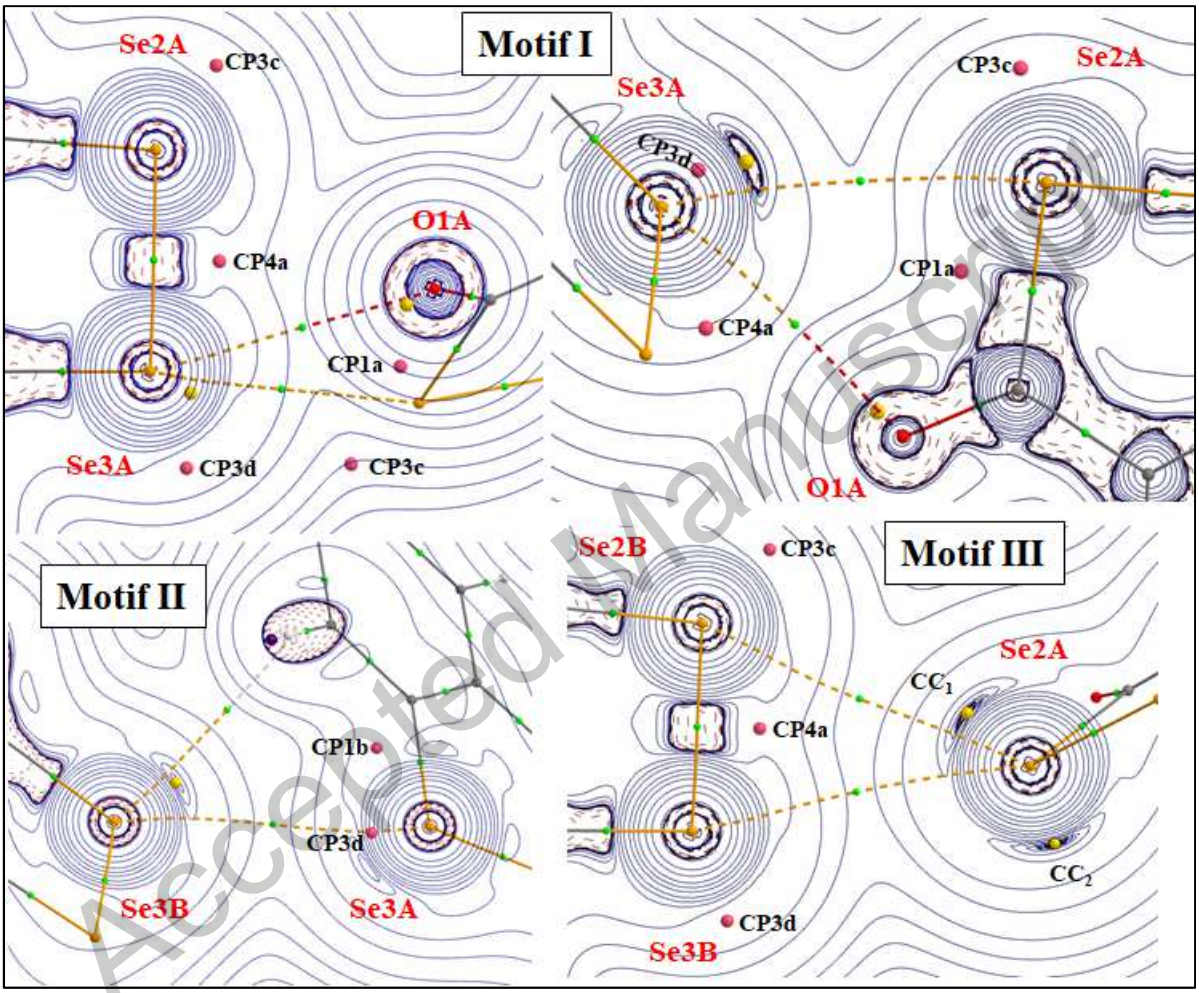

Figure 8. Intermolecular bond critical points (BCPs, small green spheres), intermolecular bond paths (dashed lines) and charge concentration and charge depletion (CC/CD) sites (yellow/pink/violet spheres) involved in the chalcogen bonding interactions present in motifs **I**, **II** and **III** of **COSeSe**, as well as a hydrogen bonding interaction in motif **II**. CPs of $L(\mathbf{r})$ are: (3,−3) in yellow , (3+1) in pink, (3,+3) in violet.

Molecular reactivity in fluoride adducts. In crystal structures, the way electrophilic-nucleophilic interactions establish can depend on several aspects, such as steric

hindrance, presence of other interactions and overall crystal packing. Therefore, it is difficult to extrapolate the reactivity behavior of this family of molecules based on crystalline features only. In order to understand the chemical reactivity around the Ch2-Ch3 bond in such dichalcogenides toward nucleophilic attack, we devised a strategy where we used the fluoride anion as a probe. Accordingly, we optimized the geometry of the eight compounds with one F^- anion sitting around the Ch2-Ch3 bond in regions R1A, R1B and R2, using the same optimization criteria's as used for monomers. The small size of F^- allows for minimum steric hindrance, while its anionic character results in a substantial nucleophilic capacity.

1. Geometry Optimization. Optimization of each molecule with F^- results in three unique true minima, each laying in one of the focused regions, namely R1A, R1B and R2 (Figure 9)

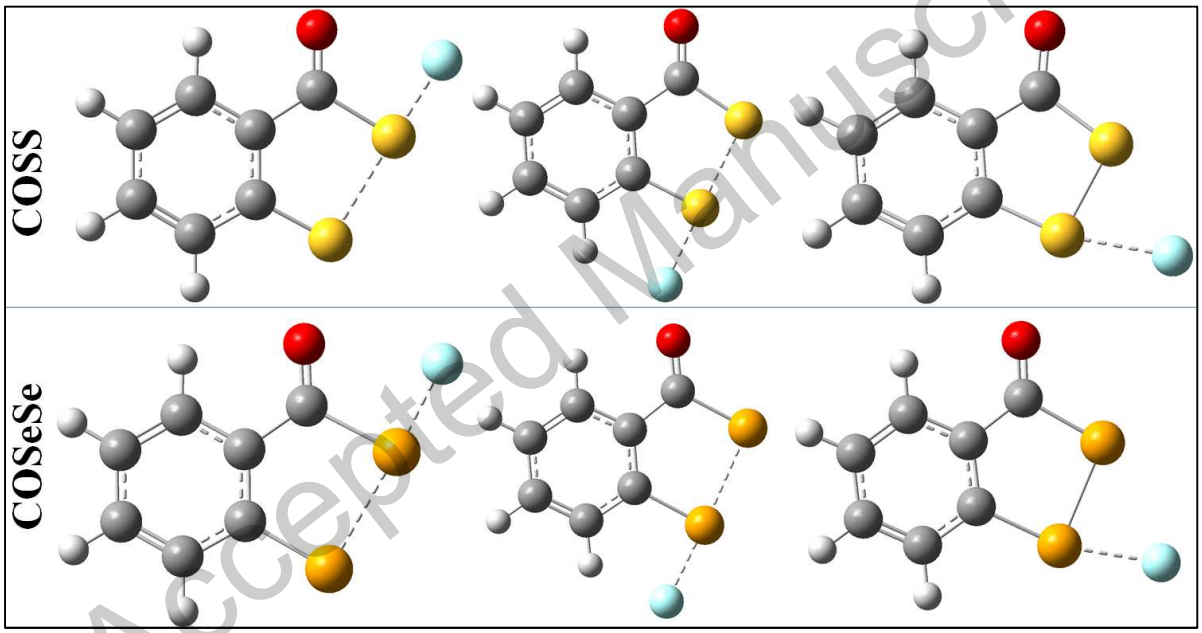

Figure 9: Optimized structure of fluoride adducts with **COSS** and **COSeSe**. The structures of other fluorine adducts were similar to that observed for **COSS** and **COSeSe**. The absence of covalent bonds between atoms should not be confused with the absence of a bonding interaction (see text). Ch•••F and Ch•••Ch bonding interactions showing $1 < |V|/G < 2$ are represented with dashed lines, whereas the rest of bonds are covalent and exhibit $|V|/G > 2$.

The optimization with F^- in the R1A region resulted in the presence of a short and almost linear evaluating the energy differences Ch3–Ch2•••F interaction in all eight adducts. The formation of the Ch2•••F bonding interaction results in the concomitant weakening of the Ch2–Ch3 bond, as evidenced from the increase in the Ch2–Ch3 bonds lengths (Table 7, Table S16). The largest

increase in distance is observed for the S−S bond, while the smallest increase is observed for the Se−Se bond. In comparison, the changes in the C1−Ch2 and C7−Ch3 bond lengths were relatively small.

Table 7. Geometrical parameters of selected fluoride adducts *via* region R1A (See Table S16 for other adducts). Units: d(Å), Δd(Å) and ∠(°).

	d (Ch2•••F)	∠ Ch3−Ch2•••F	d (Ch2−Ch3)	Δd (Ch2−Ch3)	d (C1−Ch2)	Δd (C1−Ch2)	d (C7−Ch3)	Δd (C7−Ch3)
[**COSS**•••F]$^{-1}$	1.82	179.0	2.44	+0.35	1.83	+0.00	1.73	-0.03
[**COSeSe**•••F]$^{-1}$	1.94	177.3	2.64	+0.28	1.98	0.00	1.89	-0.02
[**CSSS**•••F]$^{-1}$	1.81	173.8	2.41	+0.30	1.78	+0.03	1.72	-0.04
[**CSSeSe**•••F]$^{-1}$	1.94	177.0	2.61	+0.24	1.93	+0.03	1.88	-0.03

*Δd corresponds to the difference in the bond length observed between adduct and monomer, *i.e.* $\Delta d = d$(adduct) – d(molecule).

The results corresponding to the optimization in the R1B region are largely similar to those observed in region R1A (Tables 8 and S17). Thus, the formation of the Ch3•••F bonding interaction results in the concomitant weakening of the Ch3−Ch2 bond, as evidenced from the increase in Ch3−Ch2 bond length (Table S17). However, the stretching of the Ch2−Ch3 bond upon adduct formation is less important as compared to that observed in region R1A.

Table 8. Geometrical parameters of selected fluoride adducts *via* region R1B. (See Table S18 for other adducts). Units: d(Å), Δd(Å) and ∠(°).

	d Ch3•••F	∠ Ch2-Ch3•••F	d Ch2−Ch3	Δd Ch2−Ch3	d C1−Ch2	Δd C1−Ch2	d C7−Ch3	Δd C7−Ch3
[**COSS**•••F]$^{-1}$	1.98	178.4	2.30	+0.21	1.76	-0.07	1.77	+0.01
[**COSeSe**•••F]$^{-1}$	2.05	177.6	2.55	+0.19	1.92	-0.06	1.93	+0.02
[**CSSS**•••F]$^{-1}$	1.98	178.7	2.26	+0.15	1.72	-0.03	1.77	+0.01
[**CSSeSe**•••F]$^{-1}$	2.05	177.2	2.52	+0.15	1.87	-0.03	1.92	+0.03

*Δd corresponds to difference in the bond length observed between adduct and monomer, *i.e.* $\Delta d = d$(adduct) – d(molecule).

Strikingly, the optimization of the fluoride adducts within the R2 region does not significantly alter the molecular Ch2−Ch3, C1−Ch2 and C7−Ch3 covalent bond lengths (Table 9, Table S18). In terms of the geometrical parameters associated with the formation of either Ch2•••F or Ch3•••F bonding interaction, a clear pattern is observed. Accordingly, if Ch2 = Ch3 (*i.e.* in **COSS**, **COSeSe**, **CSSS**, **CSSeSe**), then Ch3•••F is systematically shorter than Ch2•••F, and

C7–Ch3•••F is closer to linearity than C1–Ch2•••F. For the other four adducts where Ch2 ≠ Ch3, the Ch•••F interaction is shorter and the C–Ch•••F moiety more linear with Ch = Se.

Table 9. Geometrical parameters for selected fluoride adducts via region R2. (See Table S18 for other adducts). Units: d(Å), Δd(Å) and ∠(°).

	d Ch2•••F	∠ C1–Ch2•••F	d Ch3•••F	∠ C7–Ch3•••F	d Ch2–Ch3	Δd Ch2–Ch3	d C1–Ch2	Δd C1–Ch2	d C7–Ch3	Δd C7–Ch3
[**COSS•••F**]$^{-1}$	2.57	155.6	2.25	165.2	2.09	0.00	1.79	-0.04	1.78	+0.02
[**COSeSe•••F**]$^{-1}$	2.83	145.6	2.20	164.4	2.36	+0.00	1.94	-0.04	1.96	+0.05
[**CSSS•••F**]$^{-1}$	2.51	157.4	2.25	162.6	2.08	-0.03	1.73	-0.02	1.77	+0.01
[**CSSeSe•••F**]$^{-1}$	2.75	147.9	2.21	161.5	2.34	-0.03	1.88	-0.02	1.95	+0.04

*Δd corresponds to difference in the bond length observed between adduct and monomer, *i.e.* Δd = d(adduct) – d(molecule).

2. Stability of the complexes. Twenty-four gas-phase adducts were calculated at optimized geometries. The energy of the adducts where the fluoride anion is sitting along regions R1A, R1B and R2 are respectively noted as E_{R1A}, E_{R1B} and E_{R2}. The relative stability of the complexes are discussed here by evaluating the energy differences $\Delta E_{R2\text{-}R1A} = E_{R2} - E_{R1A}$ and $\Delta E_{R2\text{-}R1B} = E_{R2} - E_{R1B}$ gathered in Table 10.

Table 10 Stability of fluoride adducts ΔE(kcal mol^{-1}) relative to those involving the R2 region

Complex	$\Delta E_{R2\text{-}R1A}$	$\Delta E_{R2\text{-}R1B}$
[**COSS•••F**]$^{-1}$	6.27	12.35
[**COSSe•••F**]$^{-1}$	-2.26	15.42
[**COSeS•••F**]$^{-1}$	12.37	6.21
[**COSeSe•••F**]$^{-1}$	7.34	12.85
[**CSSS•••F**]$^{-1}$	-0.14	10.16
[**CSSSe•••F**]$^{-1}$	-8.42	13.53
[**CSSeS•••F**]$^{-1}$	5.47	2.20
[**CSSeSe•••F**]$^{-1}$	1.90	10.53

Comparing adduct formation along regions R1B and R1A, it is found most favorable when involving the former R1B region in six out of eight molecules ($\Delta E_{R2\text{-}R1B} > \Delta E_{R2\text{-}R1A}$), while it is more stable along the latter region for only two remaining ones ($\Delta E_{R2\text{-}R1B} < \Delta E_{R2\text{-}R1A}$). For all molecules $\Delta E_{R2\text{-}R1B} > 0$, establishing that adduct formation along region R1B is

always more stable than along region R2. On the other hand, adduct formation along region R1A is more stable than along R2 ($\Delta E_{R2\text{-}R1A} > 0$) with five molecules. For two of the three remaining cases ($\Delta E_{R2\text{-}R1A} < 0$), namely [**COSSe•••F**]$^{-1}$ and [**CSSSe•••F**]$^{-1}$ adducts, the interaction Se•••F along region R2 leads to a relatively higher stability than that of S•••F along region R1A (negative $\Delta E_{R2\text{-}R1A}$). Besides, in the third case, [**CSSS•••F**]$^{-1}$, the slightly negative $\Delta E_{R2\text{-}R1A}$ value can be due to a slight repulsion between Ch1 and F^- atoms along region R1A. Altogether, among the eight most stable configurations six of them correspond to adducts formed along region R1B and two along region R1A. The two latter correspond to [**COSeS•••F**]$^{-1}$ and [**CSSeS•••F**]$^{-1}$, where the interaction Se•••F takes place with Se at Ch2 position. Hence, in all cases where adduct forms *via* the Se•••F interaction instead of the S•••F at the same position, the adduct is more stable, indicating that the former interaction is energetically more stabilizing than the latter.

3. Topology of $\rho(\mathbf{r})$ in fluoride adducts.

The topological parameters obtained at BCPs confirm a significant weakening of the Ch2–Ch3 bond when the Ch2•••F or Ch3•••F bonding formation is taking place along regions R1A or R1B, respectively (Figures S24 and S25). Indeed, the magnitudes of ρ, $\nabla^2\rho$ and $|V|/G$ for the Ch2–Ch3 bond in the adducts are significantly lower than those obtained for the monomers (Table S19 and S20). In many cases, the magnitude of ρ at the Ch2•••F (or Ch3•••F) BCP is larger than at the Ch2–Ch3 BCP within the same adduct. The $|V|/G$ descriptor for both Ch2•••F (or Ch3•••F) and Ch2–Ch3 ranges between 1 and 2 in all the complexes, demonstrating the partial covalent character of both bonding interactions after adduct formation. Comparing the results obtained for adducts formed along regions R1A and R1B, the change in the topological parameters at the Ch2–Ch3 BCP is more significant when the adduct forms *via* the region R1A, paralleling the trend previously observed with the geometrical parameters (Tables 7 and 8). One contributing factor to this feature is the additional formation of a C–H•••F hydrogen bonding interaction when the adduct formation takes place *via* the R1B region (Figure S25, Table S20), indirectly decreasing the strength of the Ch3•••F interaction that occurs simultaneously. The topological parameters clearly suggest that C–H•••F is a secondary interaction in the adduct with magnitudes ρ, $\nabla^2\rho$ and $|V|/G$ significantly lower than those observed for the stronger Ch3•••F interaction (Table S22).

On the other hand, only one Ch•••F (Ch2•••F or Ch3•••F) BCP is observed when the interaction takes place through region R2 (Figure S26). The particular occurrence of BCP is

observed depending on whether the Ch2•••F or Ch3•••F interaction is shorter and more linear within a given adduct, following the geometrical trend observed after optimization. Interestingly, the formation of either Ch2•••F or Ch3•••F bonding interaction does not lead to a weakening of the Ch2−Ch3 bond (in fact, even a slight increase in the magnitude of the topological parameters at the Ch2−Ch3 BCP is observed, Table S21). The changes in the magnitude of the different topological parameters at either C1−Ch2 or C7−Ch3 bond after adduct formation is small as compared to the changes we observed for the Ch2−Ch3 bond during the adduct formation *via* the R1A and R1B regions. In addition, the magnitudes of ρ, $\nabla^2\rho$ and |V|/G at either Ch2•••F or Ch3•••F BCP are significantly lower than those observed for the same bonding interaction when involving the R1A and R1B regions. Overall, this suggests that the Ch•••F electrophilic-nucleophilic interaction is systematically more favorable along the Ch2-Ch3 bond (R1A and R1B regions) than perpendicular to it (R2 region). This is consistent with the energy of the optimized fluoride adducts and their relative stability along regions R1A, R1B and R2. It is also important to note that the formation of Ch2•••F or Ch3•••F bonding interaction across all three regions (R1A, R1B and R2) possibly alter the hybridization of the chalcogen atom after adduct formation, as Ch2 (or Ch3) is bonded to three atoms with either partial ($1 < |V|/G < 2$) or fully covalent characteristics ($|V|/G > 2$). This would lead to a change in the hybridization of Ch2 (or Ch3) from sp^3 in monomers to partial sp^3d in adducts.

4. Topology of $L(\mathbf{r}) = -\nabla^2\rho(\mathbf{r})$. The topology of $L(\mathbf{r})$ with fluoride adducts evolves not only with respect to that of monomers at optimized geometries, but also with respect to dimers extracted from the crystal structures, as a consequence of the Ch•••F bonding formation (Figure 10, Figure S27-S29). Indeed, in adducts, the interaction between the chalcogen atom and the fluoride anion is not purely closed-shell in nature, since Ch•••F bears a partial covalent character as pointed from the topological analysis of $\rho(\mathbf{r})$. In spite of this partial shared-shell character, the $L(\mathbf{r})$ map reveals a mostly spherical VSCC region around the F-atom. The reason is twofold, (i) in the absence of a significant polarization of $\rho(\mathbf{r})$ in the bonding region, the deformation of $\rho(\mathbf{r})$ is hardly observed for chemical bonds involving fluorine atoms because of their significant electronegativity, and (ii) the large net charge of F ($q \sim -0.6\ e$) makes $\rho(\mathbf{r})$ around fluorine similar to that of an halide with partial charge. Indeed, as previously observed for I^- ($q \sim -0.5\ e$) participating in the formation of polyiodide chains,[49] here it does not rise any (3,-3) CP that could act as a nucleophilic CC site in the F-basin. Instead, this atom should be rather considered as a spherical nucleophile with net negative charge q, like I^- in polyiodide

chains. Given that both selenium and iodine atoms exhibit a fully depleted valence-shell region, the $L(\mathbf{r})$ distribution, as well as the types and disposition of CPs along the Se•••F bond path, are very similar to those observed along I•••I$^-$ bond paths in polyiodide chains, where these bonding interactions also exhibit a partial covalent character from the topology of $\rho(\mathbf{r})$.

Once the S•••F bonding interaction is established in adducts with sulfur at Ch2 (F sitting in region R1A) or at Ch3 (F sitting in region R1B) position, the reactivity surface $\nabla^2\rho(\mathbf{r}) = 0$ of sulfur shrinks (Figure 10, S27-S29), showing more open than in the corresponding optimized monomers and in dimers at crystalline geometries. Concomitantly, whereas the associated electrophilic site (CP1a or CP1b) in the open reactivity surface remains very close to the position found in monomers and dimers, the plane of charge concentration where the *lone-pairs* stand reorients around the S-atom. This reorientation can be also attributed in part to the change in the hybridization of Ch2 (or Ch3) from sp^3 (in monomers) to a partial sp^3d after adduct forms with F$^-$, accommodating the three Ch–F, C–Ch and Ch–Ch bonding interactions and the lone-pairs plane around the central Ch-atom. Hence, it shifts from the direction bisecting the angle ∠C–Ch2–Ch3 (or ∠C–Ch3–Ch2) in the monomers towards the C–S bonding direction in adducts, exceeding/approaching the C–Ch2/C–Ch3 direction (Ch2, Ch3 = S) with an angle of 14.3°/8.3° (see Figure S30). As a consequence, the CP3c-f sites that are in the close vicinity of the *lone-pairs* plane shift in a similar way in comparison to monomers (see Figure 10, S27-S29), indicating that all the electron distribution around the plane is concerned by this effect. The reorientation of the *lone-pairs* plane permits a favorable nucleophilic attack straightforwardly directed along the Ch2–Ch3 bonding direction, letting an open region that avoids the steric hindrance with *lone-pairs* and adjacent groups, as carbonyl or thiocarbonyl in region R1A or the C-C(H) moiety in region R1B. Altogether, the actual $L(\mathbf{r})$ distribution in adducts clearly shows the charge redistribution that has permitted the formation of the partial covalent bond S•••F after nucleophilic attack. At the opposite side, the Ch2–Ch3 bond is weakened because its bonding region of charge concentration shrinks, splitting in two regions, each belonging to one chalcogen atom. In addition, if the chalcogen atom that is not involved in the S•••F bond is a sulfur atom (*i.e.* in [**COSS•••**F]$^{-1}$ or [**CSSS•••**F]$^{-1}$), its reactivity surface appears more closed. On the other hand, when the nucleophilic attack takes place along region R2, the S•••F bonding interaction also shrinks the reactivity surface but significantly less that when the attack is along region R1A or R1B. At the optimized geometry, F stands closer to Ch3 (= S) and closely aligned to the C–Ch3 direction (*i.e.* in [**COSS•••**F]$^{-1}$ or [**CSSS•••**F]$^{-1}$), as the reactivity surface for Ch3 encloses a thin charge concentration region where CP2b stands, while

for Ch2 the region is thick around CP2a. On the other hand, the S•••F interaction does not affect the Ch2−S bond, which conserves its covalent character, while the charge concentration region where CP3b and *lone-pairs* stand reorients from the direction bisecting the angle ∠C−Ch3−Ch2 towards the prolongation of the Ch2−Ch3 bond, approaching the direction with an angle of 31.9° (see Figure S30). Whatever the region R1A, R1B or R2 along the adduct forms, the nucleophilic power of the CC sites increases from monomers to adducts (for example, in **COSS**, L/ρ = 9.24 and 9.74 $Å^{-2}$ for Ch2 and Ch3, and in [**COSS**···F]$^{-1}$, L/ρ = 9.97 $Å^{-2}$ for Ch2 along region R1A, and 10.23 and 9.89 $Å^{-2}$ for Ch3 along regions R1B and R2).

In the case of adducts showing the Se•••F bonding interaction along region R1A or R1B, the reactivity surface remains largely open around selenium, showing a valence-shell completely depleted and almost unchanged with respect to this in the corresponding monomers. As previously observed for the sulfur atom, the electrophilic site CP1a (or CP1b) in selenium remains very close to the position found in the monomers, while the charge concentration plane where *lone-pairs* stand reorients towards the C−Se bonding direction in adducts (exceeding/approaching the C−Se direction with an angle of 12.3°/2.5° at Ch2/Ch3 position, see Figure S31). Close to the *lone-pairs* plane, CP3a/CP3c sites at Ch2 and CP3b/CP3d sites at Ch3 also follow the same effect (Figure 10). As for S•••F, this reorientation permits the formation of the Se•••F bond straightforwardly along the Ch2−Ch3 direction after nucleophilic attack, avoiding steric hindrance with *lone-pairs* and adjacent molecular moieties. A further significant electronic effect concerns the charge concentration distribution ($\nabla^2\rho(\mathbf{r}) < 0$) in the bonding region of Ch2−Ch3, which shrinks and shifts towards the chalcogen atom that is not involved in the Se•••F bonding interaction, as a consequence of the weakening of the bond. On the other hand, when the adduct forms along region R2, similar features than those observed for S•••F show also here. Hence, F stands closer to Ch3 rather than to Ch2, while the Se•••F bonding interaction is weaker than along regions R1A and R1B and does not affect the Ch2−Se bond. Besides, the *lone-pairs* plane reorients, approaching the prolongation of the Ch2−Ch3 direction with an angle of 14.3° (see Figure S31) and letting place for the Se•••F bond. In addition, the nucleophilic power of the CC sites also increases from monomers to adducts (for example, in **COSeSe**, L/ρ = 0.16 and 0.57 $Å^{-2}$ for Ch2 and Ch3, and in [**COSeSe**···F]$^{-1}$, L/ρ = 0.70 $Å^{-2}$ for Ch2 along region R1A, and 0.99 and 0.82 $Å^{-2}$ for Ch3 along regions R1B and R2). Compared to S•••F, an increased degree of covalence exhibits for the Se•••F bonding

interaction, which indeed shows systematically larger ρ and |V|/G magnitudes at BCP when compare [**CCh1Ch2Se•••**F]$^{-1}$ to [**CCh1Ch2S•••**F]$^{-1}$ series.

It is noteworthy that the characteristics of $L(\mathbf{r})$ around S- or Se-atoms bonded to F remain mainly unchanged along the series of adducts. Thus, whatever the combination of the two other Ch-atoms in the adduct, it does not bring any significant effect on the $L(\mathbf{r})$ features around the chalcogen bonded to fluorine (Figures S27-29). For all adducts, the CPs of $L(\mathbf{r})$ around the Ch2–Ch3 bond are very similar in type and position than in monomers. Some exceptions are those close to the Ch•••F BCP or belonging to F (which are additional CPs), and those standing close to the direction bisecting the angle <C–Ch–Ch. Additional CPs can modify either the existence, the type or the position of CPs that were formerly observed in a close neighborhood in monomers, but they do not have any significant effect on the others CPs of adducts. Along Ch•••F, CPs of (3,+1) and (3,-1) type in the valence-shell of the atoms point the bonding direction.

In summary, the reorientation of the plane containing the *lone-pairs*, along with the opening, shrinking and splitting of $\nabla^2\rho(\mathbf{r}) = 0$ surfaces, are the signature of the charge redistribution that permits the nucleophilic attack to form the partial covalent bonds S•••F and Se•••F. In contrast to the observed interactions in crystalline structures, the interactions of sulfur and selenium with fluorine in adducts clearly show their not negligible degree of covalence. Indeed, in addition to the topological features of $\rho(\mathbf{r})$ already raised, the electron distribution around S- and Se-atoms significantly reorganize in adducts, leading to a an important modification of the characteristic features of $L(\mathbf{r})$ around the chalcogen atoms involved in the bonding interaction with fluorine, while in intermolecular interactions their $L(\mathbf{r})$ characteristics remain similar to those found in monomers. Thus, the electronic signature of the covalence degree of the Ch•••F bonding interaction, in not only observed from ρ and |V|/G magnitudes at BCP (significantly larger than in the molecular assembly of crystalline structures) but also from the reorientation of the plane containing the chalcogen *lone-pairs*, which appears necessary for reactivity. They are related to the anchoring geometry of Ch•••F within the adduct (aligned along the Ch2•••Ch3 direction in regions R1A and R1B, and deviated from linearity with respect to the C•••Ch direction in region R2), which seems to be the result of a minimized repulsion geometry of localized electrons (as in the *VSEPR* model) when considering the disposition of the partial covalent Ch•••F and Ch•••Ch bonding interactions, the covalent bond C•••Ch, and the lone-pairs plane, with a partial sp^3d hybridation at the central Ch-atom.

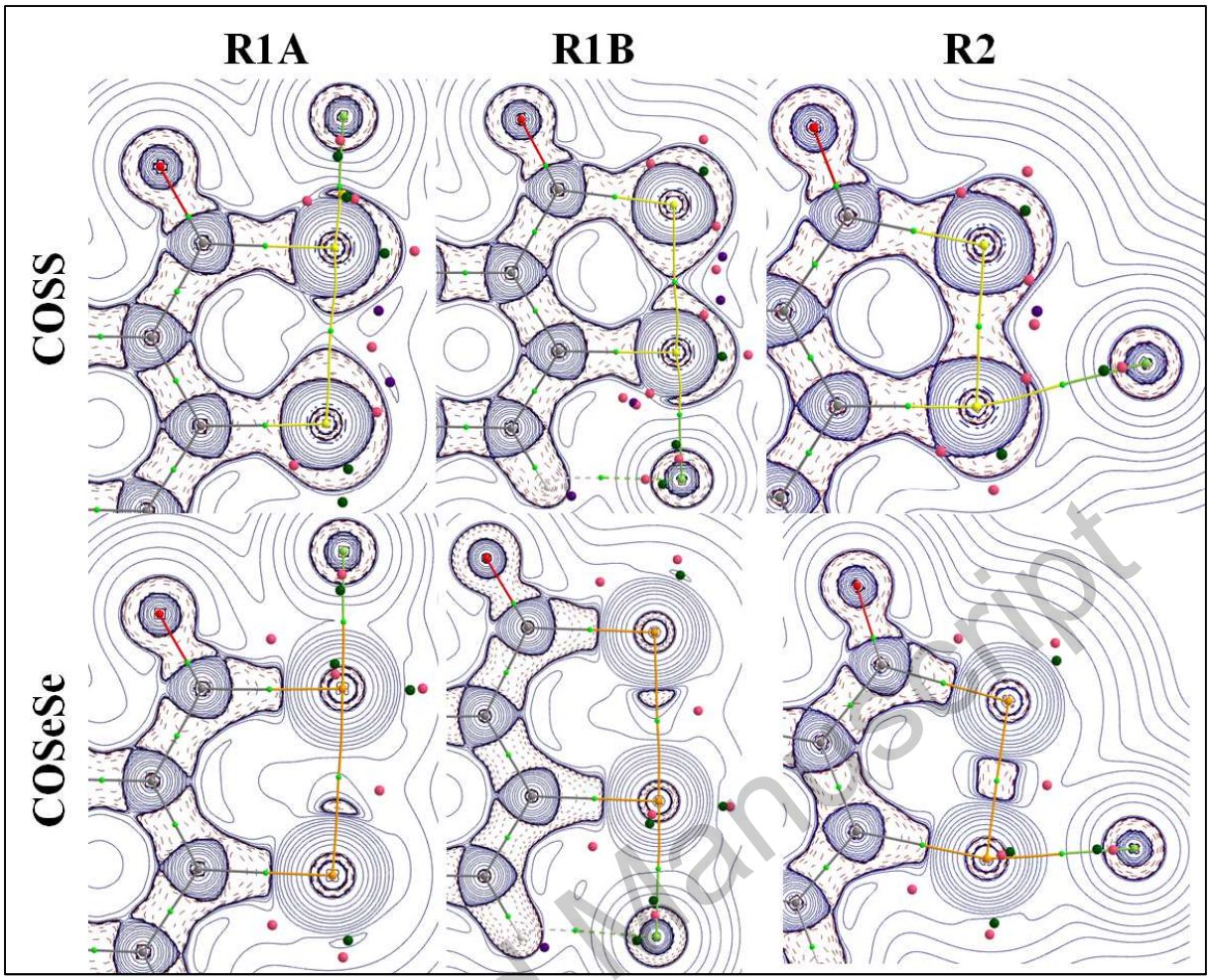

Figure 10 *L*(**r**) maps in fluoride adducts of **COSS** (top) and **COSeSe** (bottom). Bond critical points (small light green spheres), (3,+1) CPs (pink spheres) and (3,-1) CPs (dark green spheres) are depicted around Ch2, Ch3 and F atoms. A (3,+3) CP (violet sphere) is found for a H-atom that makes a hydrogen bonding interaction with F in region R1B. See Figure S22 for other adducts.

■ CONCLUSIONS

Different 3H-1,2-benzodithiol-3-(thi)one derivatives and their (mixed) selenated analogs have been used here as a model series to investigate the electrophilic character of disulfides and diselenides, which is believed to be involved both in their chemical reactivity toward nucleophiles and in their role as chalcogen bond donors in the solid state molecular assemblies. The electrostatic potential (ESP) maps clearly establish the presence of three σ-hole regions around the dichalcogenide Ch2–Ch3 bond (R1A, R1B and R2), exhibiting different amplitudes. The molecular packing of all the crystal structures is mainly driven by π-

π stacking interactions, forming columns that are interlinked to each other via hydrogen and chalcogen bonding. All the three σ-hole regions participate in the formation of chalcogen bonding interactions, with the shorter ones involving region R2.

The topologies of $\rho(\mathbf{r})$ and $L(\mathbf{r}) = -\nabla^2\rho(\mathbf{r})$ calculated at first on isolated molecules give an accurate description of electronic features associated to chalcogen atoms. The weak nature of dichalcogenide Ch2−Ch3 bond is established from the topological analysis of ρ(**r**), showing systematically lower ρ, $\nabla^2\rho$ and |V|/G values at BCP as compared to other covalent bonds. For S- and Se-atoms, the topology of $L(\mathbf{r})$ founds CC sites at chalcogen *lone-pairs* positions, and CD sites at electrophilic regions present around the Ch2−Ch3 bond. In isolated molecules, the topological CD sites of most electrophilic character are found in σ-hole regions identified by ESP maps, supporting their electrophilic description.

In the crystal structures, CD and CC sites appear face-to-face through intermolecular regions, involving σ-holes and lone-pairs. The directions of stronger CD•••CC interactions show mostly aligned to those of atoms bearing the CD and CC sites. In all crystal structures, the angle between them is typically α < ~15°, indicating that molecular orientation in the assembling is driven by these local electrostatic electrophilic•••nucleophilic interactions between CD and CC sites. Most relevant interactions involve performant CC and CD sites, which are identified by large $\Delta(L/\rho)/d^2_{CC...CD}$ values ($\Delta(L/\rho) = (L/\rho)_{CC} - (L/\rho)_{CD}$) and correspond to small α-angles. It is noteworthy that types and disposition of CPs observed for either S- or Se-atom do not change upon different intramolecular environments along the series of monomers, and only their positions modify slightly in the dimers extracted from the crystal structures. Accordingly, the topological descriptors obtained for CC and CD sites in monomers can be efficiently used for predicting molecular assemblies.

The topological descriptors of $\rho(\mathbf{r})$ confirm that all three possible σ-hole regions are involved in the assembling of molecules, with larger ρ, $\nabla^2\rho$ and |V|/G magnitudes observed at the intermolecular BCPs entailing region R2. The electrophilic power of the CD site $(L/\rho)_{CD}$ in region R2 is more important than most of those observed in regions R1A and R1B, resulting in intermolecular interactions of greater intensity. $\Delta(L/\rho)/d^2_{CC...CD}$ magnitudes also demonstrate that important electrophilic sites present along the Ch2−Ch3 bonding direction (regions R1A, R1B) are not involved in the most intense electrophilic-nucleophilic interactions, which rather concern the Ch2−Ch3 side-on interaction with a nucleophile. In molecular assemblies involving S-atoms, CD sites are accessible along the Ch2−Ch3 bonding direction in regions R1A and R1B, whereas their position in Se-atoms make them less well placed due to their proximity to

the basin of the bonded carbon atom (which can lead to steric hindrance with the C=Ch1$_{sp2}$ group), in spite they present a significantly stronger electrophilic power than S-atoms. The position of *lone-pairs* in the planes perpendicularly bisecting the ∠C−Ch−Ch angles make the electrophilic sites close around these planes less performant as anchoring sites for molecular assembling, because eventual nucleophilic centers will feel the repulsion exerted by the *lone-pairs* that are in the vicinity.

For S- and Se-atoms, the reactivity surface analysis points that nucleophilic attack is more favorable along the Ch2−Ch3 bond (regions R1A and R1B) than in perpendicular geometry (Region R2). Clearly, the involvement of CD sites in molecular assembling should be distinguished from nucleophilic attack. Indeed, while the former is mainly electrostatic with long contact distances (closed-shell interaction), in the latter, molecular electron clouds interpenetrate giving rise to a reorganization of the electron distribution that permits to generate new chemical bonds made by shared-shell interactions. Hence, although the nucleophilic attack is more difficult along a side-on approach to Ch2−Ch3 (region R2) in the absence of a hole in the reactivity surface $\nabla^2\rho(\mathbf{r}) = 0$, a significant electrostatic interaction can take place with the intermolecular environment involving this favorable electrophilic region, where the CD site and the ESP maximum appear.

Formal interaction of the 1,2-benzodithiol-3-(thi)one and their selenated analogs with the fluoride anion was used to explore the reactivity of such dichalcogenides around the Ch2−Ch3 bond toward nucleophilic attack. For all 24 optimized adducts, the Ch•••F interaction bears a partial covalent character as shown by the topological analysis of $\rho(\mathbf{r})$ ($1 < |V|/G < 2$). In spite of this partial shared-shell character, $L(\mathbf{r})$ maps reveal a mostly spherical VSCC region around the F-atom. Its significant electronegativity and net charge ($q_F \sim -0.6\ e$) make $\rho(\mathbf{r})$ around fluorine similar to that of an halide with partial charge. The characteristic topological features of $L(\mathbf{r})$ in Se•••F$^-$ show similar to those previously observed for I•••I$^-$ interactions in polyiodide chains.

Finally, the topological analysis of $L(\mathbf{r})$ in adducts points out the reorientation of the plane containing the chalcogen *lone-pairs*, along with the opening, shrinking and splitting of reactivity surfaces $\nabla^2\rho(\mathbf{r}) = 0$. They are the signature of the charge redistribution in the reactivity process that permits the nucleophilic attack. If steric hindrance with *lone-pairs* is removed by reorienting the plane they stand, the bonding interaction will take place preferably along the Ch2−Ch3 direction. Indeed, along regions R1A and R1B, all F•••Ch interactions are energetically more favorable and their bonding interactions stronger than along region R2,

where the *lone-pairs* plane is only partially reoriented, in particular with S-atoms. In all cases, the adduct is more stable when it forms through Se•••F instead of S•••F bonding interaction at the same position.

■ Experimental Section

Syntheses. *3H-1,2-Benzothiaselenol-3-one* (**COSeS**). 2,2'-Dithiodibenzoic acid (1.5 g, 5 mmol, 1 equiv.) and triphenylphosphine selenide (5 g, 15 mmol, 3 equiv.) were added to an oven dried 100 ml round bottom flask and applied high vacuum for 15-20 min. Now freshly distilled 1,4-dioxane (50 ml) was added to the round bottom flask under argon and the reaction mixture is then refluxed for 3 days by monitoring the progress of reaction using TLC. The reaction mixture is cooled down to the room temperature and filtered off the precipitated triphenylphosphine oxide as colourless crystals. The solution is concentrated using rotary vapor under reduced pressure and thus obtained crude is subjected to flash column chromatography for purification to afford **COSeS** (415 mg, 20%) as yellow solid. R_f = 0.4 (EtOAc-petroleum ether, 1:9, v/v); Mp: 80-81 °C; ^{1}H NMR (300 MHz, CDCl3): δ 7.28-7.34 (m, 1H), 7.57-7.64 (m, 2H), 7.90-7.92 (m, 1H); ^{13}C NMR (300 MHz, CDCl3): δ 125.3, 125.8, 127.6, 133.2, 133.3, 149.3, 197.3. Anal. Calcd for C_7H_4OSSe: C, 39.08; H, 1.87; S, 14.90; found: C, 40.88; H, 2.47; S, 14.55.

3H-1,2-Benzodiselenol-3-one (**COSeSe**). 2,2'-Diselenodibenzoic acid[62] (1 g, 2.5 mmol, 1 equiv.) and triphenylphosphine selenide (2.55 g, 7.5 mmol, 3 equiv.) were added to an oven dried 100 ml round bottom flask and applied high vacuum for 15-20 min. Now freshly distilled 1,4-dioxane (50 ml) was added to the round bottom flask under argon and the reaction mixture is then refluxed for 3 days by monitoring the progress of reaction using TLC. The reaction mixture is cooled down to the room temperature and filtered off the precipitated triphenylphosphine oxide as colourless crystals. The solution is concentrated using rotary vapour under reduced pressure and thus obtained crude is subjected to flash column chromatography for purification to afford **COSeSe** (130 mg, 10%) as brown solid. R_f = 0.4 (EtOAc-petroleum ether, 1:9, v/v); Mp: 90-91 °C; ^{1}H NMR (300 MHz, CDCl3): δ 7.37 (ddd, 1H, *J* = 8.0, 6.0, 2.0 Hz), 7.59-7.67 (m, 1H), 7.68-7.81 (m, 1H), 7.93 (dd, 1H, *J* = 8.0, 1.0 Hz); ^{13}C NMR (300 MHz, CDCl3): δ 125.8, 128.0, 129.8, 133.5, 134.28, 144.3, 198.0. Anal. Calcd for $C_7H_4OSe_2$: C, 32.09; H, 1.54; found: C, 34.87; H, 2.01.

*3H-1,2-Benzodithiol-3-thione (**CSSS**) and 3H-1,2-benzodithiol-3-one (**COSS**).* 2,2'-Dithiodibenzoic acid (500 mg, 1.63 mmol, 1 equiv.) and phosphorous pentasulfide (1.45 g, 3.26 mmol, 2 equiv.) were added to an oven dried 100 ml round bottom flask and applied high vacuum for 15-20 min. Now freshly distilled 1,4-dioxane (50 ml) was added to the round bottom flask under argon and the reaction mixture is then refluxed for 2 days by monitoring the progress of reaction using TLC. The reaction mixture is cooled down to the room temperature and filtered off the precipitate formed as white solid. The solution is concentrated using rotary vapor under reduced pressure and thus obtained crude is subjected to flash column chromatography for purification to afford **CSSS** (510 mg, 93%)[63] as red solid, R_f = 0.45 (EtOAc-petroleum ether, 1:9, v/v). The NMR data obtained for AD39 are in well agreement with reported one. Now to a solution containing **CSSS** (200 mg, 1.1 mmol, 1 equiv.) in $CHCl_3$ (15 ml) and CH_3COOH (10 ml), was added $Hg(OAc)_2$ (867 mg, 2.73 mmol, 2.5 equiv.) at room temperature. The reaction was then continued for 4 h. The insoluble precipitate in reaction mixture is filtered over celite and washed with DCM. The filtrate is washed with saturated $NaHCO_3$ solution x 2 and extracted with DCM. The organic layers are combined, dried over Na_2SO_4, filtered and concentrated under reduced pressure to afford **COSS** (150 mg, 82%) as dark red solid in pure form. R_f = 0.4 (EtOAc-petroleum ether, 1:9, v/v); Mp: 74-75 °C; ^{1}H NMR (300 MHz, CDCl3): δ 7.41 (ddd, 1H, *J* = 8.0, 6.0, 2.0 Hz), 7.48-7.76 (m, 2H), 7.95 (dt, 1H, *J* = 8.0, 1.0 Hz); ^{13}C NMR (300 MHz, CDCl3): δ 124.7, 125.6, 127.3, 129.1, 133.5, 148.3, 193.9. Anal. Calcd for $C_7H_4OS_2$: C, 49.98; H, 2.40; S, 38.11; found: C, 50.35; H, 2.71; S, 38.04.

*3H-2,1-Benzothiaselenol-3-thione (**CSSSe**) and 3H-2,1-benzothiaselenol-3-one (**COSSe**).* 2,2'-Diselenodibenzoic acid (500 mg, 1.25 mmol, 1 equiv.) and phosphorous pentasulfide (1.1 g, 2.5 mmol, 2 equiv.) were added to an oven dried 100 ml round bottom flask and applied high vacuum for 15-20 min. Now freshly distilled 1,4-dioxane (50 ml) was added to the round bottom flask under argon and the reaction mixture is then refluxed for 2 days by monitoring the progress of reaction using TLC. The reaction mixture is cooled down to the room temperature and filtered off the precipitate formed as white solid. The solution is concentrated using rotary vapour under reduced pressure and thus obtained crude is subjected to flash column chromatography for purification to afford **CSSSe** (450 mg, 84%) as dark red solid, R_f = 0.45 (EtOAc-petroleum ether, 1:9, v/v)); Mp: 128-129 °C; ^{1}H NMR (300 MHz, CDCl3): δ 7.49 (ddd, 1H, *J* = 8.0, 7.0, 1.0 Hz), 7.70 (ddd, 1H, *J* = 8.0, 7.0, 1.0 Hz), 7.82 (dt, 1H, *J* = 8.0, 1.0 Hz), 8.26-8.29 (m, 1H); ^{13}C NMR (300 MHz, CDCl3): δ 126.1, 126.9, 131.4, 132.7, 141.6, 151.4, 219.3. Anal. Calcd for $C_7H_4S_2Se$: C, 36.37; H, 1.74; S, 27.73; found: C, 36.40; H, 2.09; S, 27.63. To a solution containing **CSSSe** (200 mg, 0.86 mmol, 1 equiv.) in

$CHCl_3$ (9 ml) and CH_3COOH (6 ml), was added $Hg(OAc)_2$ (688 mg, 2.16 mmol, 2.5 equiv.) at room temperature. The reaction is then continued for 4 h. The insoluble precipitate in reaction mixture is filtered over celite and washed with DCM. The filtrate is washed with saturated $NaHCO_3$ solution x 2 and extracted with DCM. The organic layers are combined, dried over Na_2SO_4, filtered and concentrated under reduced pressure to afford **COSSe** (140 mg, 75%) as dark red solid in pure form. R_f = 0.4 (EtOAc-petroleum ether, 1:9, v/v); Mp: 83-84 °C; ^{1}H NMR (300 MHz, CDCl3): δ 7.45 (ddd, 1H, *J* = 8.0, 7.0, 1.0 Hz), 7.65 (ddd, 1H, *J* = 8.0, 7.0, 1.0 Hz), 7.71-7.74 (m, 1H), 7.97(dd, 1H, *J* = 8.0, 1.0 Hz); ^{13}C NMR (300 MHz, CDCl3): δ 126.1, 127.1, 127.2, 129.5, 130.5, 133.7, 194.9. Anal. Calcd for C_7H_4OSSe: C, 39.08; H, 1.87; S, 14.90; found: C, 39.12; H, 2.20; S, 15.30.

X-ray Structure Determinations. Details about data collection and solution refinement are given in Table 11. X-ray diffraction measurements were performed on a Bruker Kappa CCD diffractometer operating with a Mo Kα (λ = 0.71073 Å) X-ray tube with a graphite monochromator for all compounds except **COSeS**. The latter was collected on Bruker D8 Venture. The structures were solved (SHELXS-97) by direct methods and refined (SHELXL-97) by full-matrix least-squares procedures on F^2.[64] The 2-fold rotational disorder in **COSeS** was modelled using the PART command. All non-H atoms of the molecules were refined anisotropically, and hydrogen atoms were introduced at calculated positions (riding model), included in structure factor calculations but not refined.

Table 11 Crystallographic data.

Compound	**COSS**	**COSeSe**	**COSeS**	**COSSe**	**CSSSe**
formula	$C_{14}H_8O_2S_4$	$C_{14}H_8O_2Se_4$	$C_{14}H_8O_2S_2Se_2$	C_7H_4OSSe	$C_7H_4S_2Se$
formula moiety	$2(C_7H_4OS_2)$	$2(C_7H_4OSe_2)$	$2(C_7H_4OSSe)$	C_7H_4OSSe	$C_7H_4S_2Se$
FW (g.mol^{-1})	336.44	524.04	430.27	215.12	231.18
system	monoclinic	monoclinic	monoclinic	monoclinic	monoclinic
space group	P 2_1/c	P 2_1/c	P 2_1/c	C2/c	C2/c
a (Å)	11.0152(13)	11.0799(9)	10.9280(7)	11.5460(9)	13.0697(5)
b (Å)	8.5169(9)	8.7669(6)	8.5589(5)	8.1932(6)	7.9082(3)
c (Å)	15.3506(18)	15.5042(10)	15.2459(9)	15.5611(12)	15.3352(7)
α (deg)	90.00	90.00	90.00	90.00	90.00
β (deg)	104.094(7)	103.039(3)	102.294(2)	103.699(3)	104.060(2)
γ (deg)	90.00	90.00	90.00	90.00	90.00
V (Å^3)	1396.8(3)	1467.19(18)	1393.27(15)	1430.18(19)	1537.53(11)
T (K)	296(2)	296(2)	100(2)	296(2)	296(2)

Z	4	4	4	8	8
D_{calc} (g.cm^{-1})	1.60	2.372	2.051	1.998	1.997
μ (mm^{-1})	0.676	9.998	5.603	5.458	5.337
total refls	9383	11832	216278	8587	6594
θ_{max} (°)	27.514	27.554	52.493	27.476	27.572
abs corr	multi-scan	multi-scan	numerical	multi-scan	multi-scan
T_{min}, T_{max}	0.952, 0.967	0.142 , 0.301	0.341, 0.539	0.331, 0.721	0.208,0.808
Uniq. refls	3184	3303	16118	1636	1764
R_{int}	0.0202	0.0638	0.035	0.0375	0.0502
uniq. refls	2413	2011	12518	1260	1412
(I > 2σ(I))					
R_1	0.0361	0.0715	0.0254	0.0274	0.0355
wR_2 (all data)	0.0939	0.1303	0.0424	0.0642	0.101
GOF	1.042	1.144	1.030	1.044	1.026
res. dens. (e Å^{-3})	0.293, −0.262	1.195, −1.616	0.78, -0.66	0.458, −0.566	0.619,−0.422

■ ASSOCIATED CONTENT

Supporting Information

The Supporting Information is available free of charge on the ACS Publications website at DOI: XXXXXXXXXXXX (PDF). Topological analysis of $L(r) = -\nabla^2\rho(r)$ and supporting figures and tables (PDF). Crystallographic data for the structures (CIF) have been deposited in the Cambridge Crystallographic Data Centre. CCDC reference numbers: CCDC 2008936 to 2008939 and 2012940. These data can be obtained free of charge from The Cambridge Crystallographic Data Centre via www.ccdc.cam.ac.uk/data_request/cif

■ AUTHOR INFORMATION

Corresponding Authors

*marc.fourmigue@univ-rennes1.fr

*enrique.espinosa@univ-lorraine.fr

Notes

The authors declare no competing financial interest.

■ ACKNOWLEDGMENTS

This work has been supported by the French National Agency for Research (ANR-17-CE07-0025-01 (Nancy) and ANR-17-CE07-0025-02 (Rennes)). RS thanks the ANR for 1-year and 4-months postdoctoral contract. VV thanks the ANR and the region Grand-Est (France) for a 3-years PhD contract (supported at 50/50). AD thanks the ANR for a 3-years PhD contract. The authors thank the *EXPLOR mesocentre* for providing access to computing facilities (project 2019CPMXX0984/wbg13).

■ REFERENCES

1 Xi Zhang. In My Element: Selenium. *Chem. Eur. J.* **2019**, *25*, 2649–2650.

2 Scilabra, P.; Terraneo, G.; Resnati, G. The Chalcogen Bond in Crystalline Solids: A World Parallel to Halogen Bond. *Acc. Chem. Res*. **2019**, *52*, 1313–1324.

3 Vogel, L.; Wonner, P.; Huber, S. M. Chalcogen Bonding: An Overview. *Angew. Chem. Int. Ed.* **2019**, *58*, 1880–1891.

4 Thomas, S. P.; Satheeshkumar, K.; Mugesh, G.; Guru Row, T. Unusually Short Chalcogen Bonds Involving Organoselenium: Insights into the Se–N Bond Cleavage Mechanism of the Antioxidant Ebselen and Analogues. *Chem. Eur. J.* **2015**, *21*, 6793–6800.

5 Riel, A. M. S. ; Huynh, H.-T. ; Jeannin, O.; Berryman, O. ; Fourmigué, M. Organic selenocyanates as halide receptors: from chelation to one-dimensional systems *Cryst. Growth Des*. **2019**, *19*, 1418–1425.

6 Fourmigué, M.; Dhaka, A. Chalcogen bonding in crystalline diselenides and selenocyanates: from molecules of pharmaceutical interest to conducting materials. *Coord. Chem. Rev.* **2019**, *403*, 213084.

7 Bhabak, K. P.; Mugesh, G. Amide-Based Glutathione Peroxidase Mimics: Effect of Secondary and Tertiary Amide Substituents on Antioxidant Activity. *Chem. Asian J.* **2009**, *4*, 974–983.

8 Livinghouse, T.; Back, T. G. N-Phenylselenophthalimide. *e-EROS* **2004**, 1–5.

9 Roebuck, B. D.; Curphey, J. J.; Li, Y.; Baumgartner, K. J.; Bodreddigary, S.; Yan, J.; Gange, S. J.; Kensler, T. W.; Sutter, T. R. Evaluation of the cancer chemopreventive potency of dithiolethione analogs of oltipraz. *Carcinogenesis* **2003**, *24*, 1919–1928.

[10] Brezgunova, M.; Lieffrig, J.; Aubert, E.; Dahaoui, S. ; Fertey, P. ; Lebègue, S.; Angyan,J. ; Fourmigué, M. ; Espinosa E. Chalcogen Bonding: Experimental and Theoretical Determinations from Electron Density Analysis – Geometrical Preferences Driven by Electrophilic-Nucleophilic Interactions. *Cryst. Growth Design* **2013**, *13*, 3283–3289.

[11] Garrett, G. E.; Carrera, E. I.; Seferos, D. S.; Taylor, M. S. Anion recognition by a bidentate chalcogen bond donor. *Chem. Commun*. **2016**, *52*, 9881–9884.

[12] Ho, P. C.; Szydlowski, P.; Sinclair, J.; Elder, P. J. W.; Kübel, J.; Gendy, C.; Lee, L. M.; Jenkins, H.; Britten, J. F.; Morim, D. R.; Vargas-Garcia, I. Supramolecular macrocycles reversibly assembled by Te•••O chalcogen bonding. *Nat. Commun*. **2016**, *7*, 11229.

[13] Benz, S. ; Lopez-Andarias, J.; Mareda, J. ; Sakai, N.; Matile, S. Catalysis with Chalcogen Bonds. *Angew. Chem. Int. Ed.* **2017**, *56*, 812–815.

[14] Huynh, H.-T. ; Jeannin, O.; Fourmigué, M. Organic selenocyanates as strong and directional chalcogen bond donors for crystal engineering. *Chem. Commun.* **2017**, *53*, 8467–8469.

[15] Jeannin, O.; Huynh, H.-T. ; Riel, A. M. S.; Fourmigué, M. Chalcogen bonding interactions in organic selenocyanates: from cooperativity to chelation. *New J. Chem*. **2018**, *42*, 10502–10509.

[16] Kang, J. M.; Ferrell, A. J; Chen, W.; Wang, D. F.; Xian, M. Cyclic Acyl Disulfides and Acyl Selenylsulfides as the Precursors for Persulfides (RSSH), Selenylsulfides (RSeSH), and Hydrogen Sulfide (H_2S). *Org. Lett.* **2018**, *20*, 852–855.

[17] Salvetti, R.; Martinetti, G.; Ubiali, D.; Pregnolato, M.; Pagani, G. 1,2-Dithiolan-3-ones and derivatives structurally related to leinamycin. Synthesis and biological evaluation. *Il Farmaco* **2003**, 58, 995–998.

[18] Iyer, R. P.; Phillips, L. R.; Egan, W.; Regan, J. B.; Beaucage, S. L. The automated synthesis of sulfur-containing oligodeoxyribonucleotides using 3*H*-1,2-benzodiothiol-3-one 1,1-dioxide as a sulfur-transfer reagent. *J. Org. Chem.* **1990**, *55*, 4693-4699.

[19] Marchan, V.; Gibert, M.; Messeguer, A.; Pedroso, E.; Grandas, A. Use of Dimethyldioxirane for the Oxidation of 1,2-Dithiolan-3-ones to 1-Oxides or 1,1-Dioxides. Preparation of 3*H*-1,2-Benzodithiol-3-one 1,1-Dioxide (Beaucage Sulfurizing Reagent). *Synthesis* **1999**, 43–45.

[20] Adam, W.; Zhao, C.-G.; Jakka, K. In: *Oxidation of Organic Compounds by Dioxiranes*, by Adam, W.; Zhao, C.-G.; Saha-Möller, C. R.; Jakka, K. 2009, Chp 2, pp 313-662, Organic Reactions, Inc. John Wiley & Sons.

[21] Iyer, R. P.; Egan, W.; Regan, J. B.; Beaucage, S. L. 3*H*-l,2-Benzodithiole-3-one 1,1-Dioxide as an Improved Sulfurizing Reagent in the Solid-Phase Synthesis of Oligodeoxyribonucleoside Phosphorothioates. J. *Am. Chem. Soc*. **1990**, *112*, 1254−1255.

[22] Iyer, R. P.; Phillips, L. R.; Egan, W.; Regan, J. B.; Beaucage, S. L. The Automated Synthesis of Sulfur-Containing Oligodeoxyribonucleotides Using 3/7-l,2-Benzodithiol-3-one 1,1-Dioxide as a Sulfur-Transfer Reagent. *J. Org. Chem*. **1990**, *55*, 4693−4699.

[23] Stawinski, J.; Thelin, M. Nucleoside H-phosphonates. 14. Synthesis of nucleoside phosphoroselenoates and phosphorothioselenoates via stereospecific selenization of the corresponding H-phosphonate and H-phosphonothioate diesters with the aid of new selenium-transfer reagent, 3H-1,2-benzothiaselenol-3-one. *J. Org. Chem*. **1994**, *59*, 130−136.

[24] Stawinski, J.; Thelin, M. 3H-1,2-benzothiaselenol-3-one – A new selenizing reagent for nucleosode H-phosphonate and H-phosphonothioate diesters. *Tet. Lett.* **1992**, *33*, 7255−7258.

[25] Lin, L.; Caton-Williams, J.; Kaur, M.; Patino, A. M.; Sheng, J.; Punetha, J.; Huang, Z. Facile synthesis of nucleoside 5 '-(alpha-P-seleno)-triphosphates and phosphoroselenoate RNA transcription. *RNA* **2011**, 17, 1932−1938.

[26] Klingsberg, E. US Patent Office, 1970, US 3,511,853

[27] Van Caneghem, P. Comparative effects of selenium compounds and their sulfur analogs on the stability of lysosomes and mitochondria in vitro. *Biochem. Pharmacololy.* **1974**, 23, 3491−3500.

[28] Ogurtsov, V. A.; Karpychev, Y. V.; Nelyubina, Y. V.; Primakov, P. V.; Koutentis, P. A.; Rakitin, O. A. Synthesis of 6,7-Dihydropyrrolo[2,1-c][1,3]thiazino[3,2-a]pyrazine-4(11bH)-(thi)ones from 1,2-Dithiolo-3-(thi)ones. *Eur. J. Org. Chem.* **2019**, 4149–4158.

[29] Jin, H.; Jiang, D.; Gao, J.; Qiang, G.; Gong, Y. A facile synthesis of 3H-benzo[1,2]dithiole-3-thiones and their condensation with active methylene compounds. *Phosphorus, Sulfur and Silicon and the Related Elements* **2011**, 186, 2341−2349.

[30] Boukebbous, K.; Lalfa, El-Adoui; F., Khelifi, T.; Kermandji, A. M. H. Study on the tin(IV) complex of 4,5-benzo-1,2-dithiole-3-thione with IR, chemical analysis, and theory. *J. Chem Chem. Eng.* **2011**, *5*, 818−823.

[31] Latif, N.; Nada, A.; El-Namaky, H. M.; Haggag, B. Carbonyl and thiocarbonyl compounds. Part XVI. Cleavage of spiro[1,3-benzodioxole-2,3'(H)-1,2-benzodithiole] with nucleophilic reagents. *Ind. J. Chem. B* **1979**, *18*, 131−135.

[32] Chen, W.; Liu, C.; Peng, B.; Zhao, Y.; Pacheco, A.; Xian, M. New fluorescent probes for sulfane sulfurs and the application in bioimaging. *Chem. Sc.* **2013**, *4*, 2892−2896.

[33] Liu, C.; Chen, W.; Shi, W.; Peng, B.; Zhao, Y.; Ma, H.; Xian, M.Rational Design and Bioimaging Applications of Highly Selective Fluorescence Probes for Hydrogen Polysulfides *J. Am. Chem. Soc.* **2014**, *136*, 7257−7260.

[34] Schmidt, U. Trithiones XIV. Replacement of a heteroatom in rings with two neighboring heteroatoms. *Justus Liebigs Ann. Chem.* **1960**, *635*, 109−118.

[35] Oae, S.; Sakaki, K.; Fukumura, M.; Tamagaki, S.; Matsuura, Y.; Kakudo, M. Preparation and assignment of selenium analogs of benzo-1,2-dithiole-3-thione. *Heterocycles* **1982**, *19*, 657−661.

[36] AIMAll (Version 19.10.12), Todd A. Keith, TK Gristmill Software, Overland Park KS, USA, 2019 (aim.tkgristmill.com)

[37] Gaussian 09, Revision A.02, M. J. Frisch, G. W. Trucks, H. B. Schlegel, G. E. Scuseria, M. A. Robb, J. R. Cheeseman, G. Scalmani, V. Barone, G. A. Petersson, H. Nakatsuji, X. Li, M. Caricato, A. Marenich, J. Bloino, B. G. Janesko, R. Gomperts, B. Mennucci, H. P. Hratchian, J. V. Ortiz, A. F. Izmaylov, J. L. Sonnenberg, D. Williams-Young, F. Ding, F. Lipparini, F. Egidi, J. Goings, B. Peng, A. Petrone, T. Henderson, D. Ranasinghe, V. G. Zakrzewski, J. Gao, N. Rega, G. Zheng, W. Liang, M. Hada, M. Ehara, K. Toyota, R. Fukuda, J. Hasegawa, M. Ishida, T. Nakajima, Y. Honda, O. Kitao, H. Nakai, T. Vreven, K. Throssell, J. A. Montgomery, Jr., J. E. Peralta, F. Ogliaro, M. Bearpark, J. J. Heyd, E. Brothers, K. N. Kudin, V. N. Staroverov, T. Keith, R. Kobayashi, J. Normand, K. Raghavachari, A. Rendell, J. C. Burant, S. S. Iyengar, J. Tomasi, M. Cossi, J. M. Millam, M. Klene, C. Adamo, R. Cammi, J. W. Ochterski, R. L. Martin, K. Morokuma, O. Farkas, J. B. Foresman, and D. J. Fox, Gaussian, Inc., Wallingford CT, 2016.

[38] Bader, R. F. W. Atoms in Molecules − A Quantum Theory; Clarendon: Oxford, 1990

[39] Espinosa, E; Molins, E; Lecomte, C. Hydrogen bond strengths revealed by topological analyses of experimentally observed electron densities. *Chem. Phys. Lett*. **1998**, *285*, 170−173.

[40] Espinosa, E; Alkorta, I; Elguero, J; Molins E. From weak to strong interactions: A comprehensive analysis of the topological and energetic properties of the electron density distribution involving X−H•••F−Y systems. *J. Chem. Phys*. **2002**, *117*, 5529−5542.

[41] Malcom, N. O. J.; Popelier, P. L. A. The full topology of the Laplacian of the electron density: scrutinising a physical basis for the VSEPR model. *Faraday Discuss.* **2003**, *124*, 353-363.

[42] Popelier, P. L. A. On the full topology of the Laplacian of the electron density. *Coord. Chem. Rev.* **2000**, *197*, 169-189.

[43] Brezgunova, M. E.; Aubert, E.; Dahaoui, S.; Fertey, P.; Lebegue, S.; Jelsch, C.; Angyan, J. G.; Espinosa, E. Charge Density Analysis and Topological Properties of Hal3-Synthons and Their Comparison with Competing Hydrogen Bonds. *Cryst. Growth Des.* **2012**, *12*, 5373-5386.

[44] Amezaga, N. J. M.; Pamies, S. C.; Peruchena, N. M.; Sosa, G. L. Halogen Bonding: A Study based on the Electronic Charge Density. *J. Phys. Chem. A* **2010**, *114*, 552-562.

[45] Eskandan, K.; Mahmoodabadi, N. Pnicogen Bonds: A Theoretical Study Based on the Laplacian of Electron Density. *J. Phys. Chem. A* **2013**, *117*, 13018-132024.

[46] Duarte, D. J. R.; Peruchena, N. M.; Alkorta, I. Double Hole–Lump Interaction between Halogen Atoms. *J. Phys. Chem. A* **2015**, *119*, 3746-3752.

[47] Eskandari, K.; Zariny, H. Halogen bonding: A lump–hole interaction. *Chem. Phys. Lett.* **2010**, *492*, 9-13.

[48] Khavasi, H. R.; Gholami, A.; Hosseini, M.; Nikpoor, L.; Eskandari, K. Complementary Features of Inorganic (M–X) and Organic (C–X′) Halogens in C–X′···X–M Halogen Bonds: A Study Based on Structure, Energy, and Topological Electron Density. *Cryst. Growth Des*. **2020**, *20*, 2266-2274.

[49] Lamberts, K.; Handels, P.; Englert, U.; Aubert, E., Espinosa, E. Stabilization of polyiodide chains via anion···anion interactions: experiment and theory. CrystEngComm 2016, 18, 3832–3841.

[50] Boukebbous, K.; Laifa, E. A.; De Mallmann, A. 3H-1,2-Benzodi-thiole-3-thione. *IUCrData* **2016**, *1*, x161688.

[51] Boukebbous, K.; Laifa, E. A. ; De Mallmann, A. ; Taoufik, M. A second polymorph of 3H-1,2-benzodi-thiole-3-thione. *IUCrData* **2016**, *1*, x161799.

[52] Oae, S.; Sakaki, K.; Kakudo, M. Preparation and assignment of selenium analogs of benzo1,2-dithiole-3-thione. *Heterocycles* **1982**, *19*, 657–661.

[53] Bondi. A. Van der Waals volumes and radii. *J. Phys. Chem.* **1964**, *68*, 441–451.

[54] Murray, J. S.; Lane, P.; Politzer, P. Expansion of the sigma-hole concept. *J. Mol. Model.* **2009**, *15*, 723–729.

[55] Dmitrenko, O.; Thorpe, C.; Bach, R. D. Mechanism of SN2 disulfide bond cleavage by phosphorus nucleophiles. Implications for biochemical disulfide reducing agents. *J. Org. Chem.* **2007**, *72*, 8298–8307.

[56] Dopieralski, P.; Arino, J. R.; Anjukandi, P.; Krupicka, M.; Kiss, J.; Marx. D. The Janus-faced role of external forces in mechanochemical disulfide bond cleavage. *Nat. Chem.* **2013**, *5*, 685;
[57] Levron, B.; Burgot, G.; Burgot, J.-L. On the reduction of dithiolethiones and dithiolylium ions by NADPH and glutathione reductase. *Arch. Biochem. Biophys*. **2000**, *382*, 189−194.
[58] Parker, A. J.; Kharasch, N. Derivatives of Sulfenic Acids. XXXVI. The Ionic Scission of the Sulfur-Sulfur Bond.[1] Part 1. *J. Am. Chem. Soc*. **1960**, *82*, 3071−3075.
[59] Douglass, I. B. Some New Reactions of Methanesulfenyl Chloride. *J. Org. Chem*. **1959**, *24*, 2004−2006.
[60] Bachrach, S. M.; Demoin, D. W.; Luk, M.; Miller, J. V. Nucleophilic attack at selenium in diselenides and selenosulfides. A computational study. *J. Phys. Chem. A*. **2004**, *108*, 4040−4046.
[61] Heverly-Coulson, G. S.; Boyd, R. J.; Mó, O.; Yáñez, M. Revealing Unexpected Mechanisms for Nucleophilic Attack on S−S and Se−Se Bridges. *Chem. Eur. J*. **2013**, *19*, 3629−3638.
[62] Kamigata, N.; Iizuka, H.; Izuoka, A.; Kobayashi, M. Photochemical Reaction of 2-Aryl-1,2-benzisoselenazol-3(2H)-ones. *Bull. Chem. Soc. Jpn*., **1986**, *59*, 2179−2183.
[63] Stammer, X.; Tonigold, K.; Bashir, A.; Kafer, D.; Shekhah, O.; Hulsbusch, C.; Kind, M.; Groß, A.; Woll, C. A highly ordered, aromatic bidentate self-assembled monolayer on Au(111): a combined experimental and theoretical study. *Phys. Chem. Chem. Phys*., 2010, **12**, 6445–6454.
[64] Sheldrick, G. M. Programs for the Refinement of Crystal Structures; University of Göttingen: Göttingen, Germany, 1996.

For Table of Contents Use Only

Understanding Reactivity and Assembly of Dichalcogenides: Structural, Electrostatic Potential and Topological Analyses of 3*H*-1, 2-Benzodithiol-3-one and Se Analogs

Rahul Shukla,[†] Arun Dhaka,[‡] Emmanuel Aubert,[†] Vishnu Vijayakumar-Syamala,[†] Olivier Jeannin,[‡] Marc Fourmigué*,[‡] and Enrique Espinosa*,[†]

[†] *Université de Lorraine, CNRS, CRM2, F-54000 Nancy, France. E-mail: enrique.espinosa@univ-lorraine.fr*

[‡] *Université de Rennes, CNRS, ISCR (Institut des Sciences Chimiques de Rennes), UMR 6226, Campus de Beaulieu, F-35042 Rennes, France. E-mail: marc.fourmigue@univ-rennes1.fr*

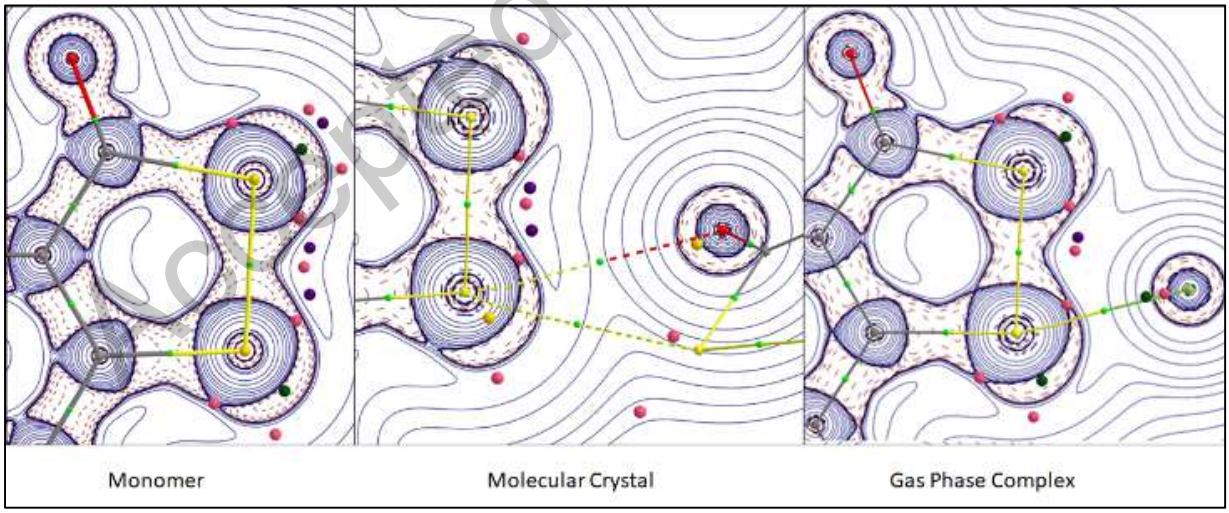

Exploring the molecular assembly and reactivity around Ch-Ch bonds (Ch = S, Se) in dichalcogenide molecules